Version 3.51, March 2005 DØ Note 4749

Measurement of $\sigma(p\bar{p} \rightarrow WX) \times \mathrm{Br}(\mathrm{W} \rightarrow \mu\nu)$ at $\sqrt{s} = 1.96$ TeV

Frédéric Déliot[a], **Gavin Hesketh**[b], **Paul Telford**[c], **Boris Tuchming**[a]

[a] DAPNIA/SPP, CEA-Saclay, France
[b] Northeastern University, USA
[c] University of Manchester, UK

Abstract

A measurement of the cross-section for W production times the branching ratio for $\mathrm{W} \rightarrow \mu\nu$ in $\mathrm{p\bar{p}}$ collisions at $\sqrt{s} = 1.96$ TeV is described. The measurement is performed using a data sample corresponding to an integrated luminosity of 95.6 pb^{-1} collected at the Tevatron with the DØ experiment between February 2003 and September 2003. A total of 62,285 candidate isolated muon events are selected with estimated background of 1.0% arising from $\mathrm{b\bar{b}}$ and in-flight meson decays, and 6.8% arising from $\mathrm{Z} \rightarrow \mu^+\mu^-$, $\mathrm{Z} \rightarrow \tau^+\tau^-$ and $\mathrm{W} \rightarrow \tau\nu$ decay. The result obtained is:

$$\sigma(p\bar{p} \rightarrow WX) \times \mathrm{Br}(\mathrm{W} \rightarrow \mu\nu) = 2989 \pm 15(\mathrm{stat}) \pm 81(\mathrm{syst}) \pm 194(\mathrm{lumi}) \;\; \mathrm{pb}.$$

Contents

1 Introduction

A measurement of the cross-section for W Boson production times the branching ratio for $\mathrm{W} \rightarrow \mu\nu$ in $\mathrm{p\bar{p}}$ collisions at 1.96 TeV using 95.6 $\mathrm{pb}^{-1}$of data is described [1].

The production of W Bosons at the Tevatron is dominated by quark-antiquark fusion, as show in Fig. 1. Gluon bremsstrahlung in the initial state can produce one or more jets of hadrons in the collision, but in general W events are fairly low occupancy. A $\mathrm{W} \rightarrow \mu\nu$ event is characterised by a high energy muon and high missing transverse energy ($\not\!\!E_{\mathrm{T}}$), which indicates the presence of a neutrino.

The main backgrounds come from other decays of W and Z Bosons ('electroweak' background), semi-leptonic quark decays (QCD background), cosmic ray muons and muons from the in-flight decays of pions and kaons. The "electroweak background" is evaluated with the same Monte Carlo simulation used to measure the acceptance. All other backgrounds are evaluated using the data.

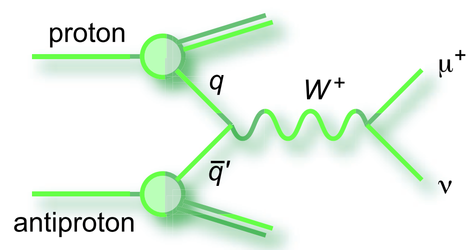

Figure 1: Dominating Feynman diagram for W production at Tevatron.

The rest of this Note is structured as follows. In Section 2 the event selection criteria are described. In Section 3 the efficiencies for $\mathrm{W} \rightarrow \mu\nu$ events to pass the event selection are computed. In Section 4 the method used to obtain the acceptance is detailed, concentrating on a description of the fast Monte Carlo simulation. In Section 5, the fraction of the candidate events attributable to background is evaluated. Finally, Section 6 describes the calculation of the cross section measurement and compares the data with Monte Carlo predictions.

2 Selection of $\mathrm{W} \rightarrow \mu\nu$ Events

The event selection requires evidence that a high transverse momentum (p_T) muon and a neutrino are produced. The muon is identified by requiring presence of a track in the central detector that is matched to a track of at least 'medium' quality [2] in the muon chambers. In order to ensure a reasonable trigger and reconstruction efficiencies, the muons are required to be within the geometric acceptance of the muon chambers that is defined to exclude the forward region around the beam pipe and the region of the bottom gap.

The neutrino is identified by missing transverse energy ($\not\!\!E_{\mathrm{T}}$). To obtain the $\not\!\!E_{\mathrm{T}}$, the vector sum of the energy, calculated from the angles of the energy deposited in the calorimeter, is

[1] This is an update on a previous preliminary measurement performed in DØ in March 2003 using 17 pb^{-1} [1].

corrected for the momentum of the muon, as measured in the central tracking system. This vector is inverted to give the $\not\!\!E_T$. Since W events contain a low number of tracks the primary vertex finding probability has been estimated to be only 90-95% in these events. In order not to be affected by this inefficiency the $\not\!\!E_T$ is re-calculated using the z coordinate of the track matched to the muon at the point of closest approach to the beam axis.

In order to reduce the $b\bar{b}$ background, the muon is required to be isolated from other particles in both the calorimeter and the central tracker. There is a background from mesons, such as pions and kaons, that decay in the central tracker (In-flight decays). This produces a kinked track at the point of decay, which affects the central track reconstruction, as well as the momentum resolution. This background is reduced by quality cuts on the central track, in particular on the distance of closest approach of the track to the beam, and the fit χ^2/d.o.f. of the central track.

To remove both the cosmic ray and $Z \rightarrow \mu^+\mu^-$ backgrounds, events are vetoed if there is another reconstructed muon, or if there is a second high p_T track in the event. The full event selection cuts are listed below, with further discussion and plots following.

2.1 Data Sample

The analysis was performed on data recorded between February and September 2003 ($173516 \leq$ run number ≤ 180956). The total DØ recorded luminosity for this run range is $\simeq 117$ pb^{-1}. This data has been processed with version p14 of the DØ reconstruction program and run through the pass-1 fixer program. This analysis used the Common Samples single muon skim *1MUloose* [3]. This skim requires at least one 'loose' quality muon with either p_T from the 'local' muon system or from a combined fit of the central track and 'local' muon system greater than 8 GeV/c.

Runs collected before February 2003 did not have Level 3 trigger information read out, complicating trigger efficiency measurement. These runs are not used, leading to a loss of approximately 27 pb^{-1}. No further data is added as this analysis is not really limited by statistics.

Runs declared as having bad data quality according to the SMT, CFT, CAL and Muon groups are removed. Luminosity blocks declared bad by the luminosity, jet and missing transverse energy groups are removed as well. In addition, it was found that the beam position changed during run 180211 which interfered with the distance of closest approach measurement. This run is also removed.

The total DØ recorded luminosity for the remaining data sample amounts to $\simeq 96.4$ pb^{-1}.

2.2 Triggers and Luminosity

There are two single muon triggers, both from Trigger lists V10.30 to V12.30, used in this analysis, namely MUW_A_L2M3_TRK10 and MUW_W_L2M3_TRK10.

For MUW_W_L2M3_TRK10, the trigger requires :

- at Level 1: at least one muon trigger in the "wide region" (detector $|\eta| < 1.5$) with tight scintillator and loose wire requirements (mu1ptxwtlx_ncu)
- at Level 2: at least one Level 2 medium muon with $p_T > 3$ GeV/c.

- at Level 3: at least one Level 3 central track with $p_T > 10$ GeV/c.

MUW_A_L2M3_TRK10 is the same trigger except that the Level 1 trigger term benefits from the full muon detector coverage: mu1ptxatlx_ncu is "all region").

For each run, one of these triggers is selected, depending on the prescales. When the "wide" region trigger has a lower prescale it is selected. When the prescales are equal, the "all" region trigger is selected to take advantage of the larger acceptance. Note that the "all" region trigger never has a lower prescale than the "wide" region trigger. The prescale of the latter is 1 ($\simeq 98\%$) of the time.

The data is split into two samples. In the following we will refer to them as the MUW_W_L2M3_TRK10 sample and the MUW_A_L2M3_TRK10 sample. Their respective luminosities are :

- for MUW_W_L2M3_TRK10 $\mathcal{L} = 53.7$ pb^{-1}
- for MUW_A_L2M3_TRK10 $\mathcal{L} = 41.9$ pb^{-1}

which correspond to a total luminosity of 95.6 pb^{-1}. The relative uncertainty on these numbers amounts to 6.5% [4].

2.3 Event Selection

To select W $\rightarrow \mu\nu$ candidate events the following cuts are applied:

1. Events are required pass one of the single muon triggers: MUW_W_L2M3_TRK10 or MUW_A_L2M3_TRK10, as explained in Section 2.2.

2. Events are required to contain one 'medium' quality muon matched to a central detector track with p_T greater than 20 GeV/c.

3. The muon is required to be within the nominal geometric acceptance of the muon detector, defined by requiring:

   (a) $|x|$ or $|y| > 110$ cm to exclude the forward region around the beam pipe;

   (b) $|\eta| > 1.25$ for $4.25 < \phi < 5.15$ to exclude the "bottom hole" in the muon system,

   where x, y, η and ϕ are *local* muon track coordinates, measured at the muon system A-layer. Note that the 'wide' region single muon trigger covers $|\eta_{\mathrm{local}}| < 1.5$, placing a further limit on the acceptance when this trigger is used. However, no additional explicit cut is placed on η.

4. The muon is required to be isolated in the calorimeter and central tracking detector, satisfying the isolation conditions:

   (a) $\Sigma_{halo}(E_T) < 1.65 + 0.75 \times \mathcal{L}_{\mathcal{I}}$ GeV, where $\mathcal{L}_{\mathcal{I}}$ is the instantaneous luminosity[2] per crossing (in units of 10^{30}cm^{-2}s^{-1}), and $\Sigma_{halo}(E_T)$= $\Sigma_{cone0.4}(E_T)$- $\Sigma_{cone0.1}(E_T)$, with

[2] A typical value in our sample is $\mathcal{L}_{\mathcal{I}} = 0.6 \times 10^{30}$cm^{-2}s^{-1}.

$\Sigma_{cone0.1}(E_T)$ and $\Sigma_{cone0.4}(E_T)$ being sums of the E_T of calorimeter clusters in cones of $\Delta R = 0.1$ and $\Delta R = 0.4$ around the muon. In forming these sums, only cells in the electromagnetic and fine hadronic calorimeters are used, not those in the coarse hadronic calorimeter.

(b) $\Sigma_{cone0.5}(p_T) < 1.1 + 0.5 \times \mathcal{L_I}$ GeV/c, where $\Sigma_{cone0.5}(p_T)$ is the sum of p_T of tracks contained within a cone of width $\Delta R < 0.5$ around the muon direction. In forming this sum, all tracks originating within 2 cm of the track matched to the muon in the z direction along the beam axis are considered and the track matched to the muon is excluded.

The choice of these requirements is discussed in the appendix part page 60.

5. Missing transverse energy corrected for the medium muon p_T,$\not\!\!E_{\rm T}$> 20 GeV. The transverse energy is computed with respect to the z of the muon at the beam axis.

6. The transverse mass, M_T> 40 GeV/c^2. The transverse mass is calculated using equation 1:

$$M_T = \sqrt{(\not\!\!E_{\rm T} + p_T)^2 - (\not\!\!E_{\rm x} + p_x)^2 - (\not\!\!E_{\rm y} + p_y)^2} \qquad (1)$$

where p_T, p_x and p_y are the transverse, x and y components of the muon momentum. This cut rejects few events ($\simeq 0.4\%$), but does so in a region in which the semi-leptonic decay background proved difficult to estimated (In events with low M_T the muon and $\not\!\!E_{\rm T}$ are close together).

7. The central track is required to have at least one hit in the silicon (SMT) tracker. A gain of approximately 15% in the number of W $\rightarrow \mu\nu$ events could be recovered by removing the SMT requirement, but these events suffer from significantly high in-flight decay backgrounds, and so are not used in this analysis.

8. $|dca| < 110$ μm, where dca is the distance of closest approach of the muon track to the beam position in the x-y plane. The beam position is measured on a run by run basis by the DØ tracking algorithm [5]. This cut is effective at removing both in-flight decay and cosmic ray backgrounds.

9. χ^2/d.o.f. < 3.3, where χ^2/d.o.f. is that of the central track. This cut is effective at removing in-flight decay backgrounds and poorly reconstructed tracks.

10. As a veto against Z $\rightarrow \mu^+\mu^-$ and cosmic rays, events are rejected if there is another medium quality muon with $|nseg| = 3$ in the event (with or without a matched track) separated in ϕ from the selected muon: $\Delta\phi(\mu, \mu_{veto}) > 0.1$. Events with a second central track with p_T greater than 20 GeV/c that passes the track quality cuts used by the W $\rightarrow \mu\nu$ analysis with $\Delta\phi > 2.1$ between the two tracks are also rejected. This cut is discussed in more detail in Section 3.6.

11. The muon track is required to be within $\Delta\phi < 0.5$ of a Level 3 track with $p_T > 10$ GeV/c. This cut is added for consistency with the Level 3 tracking efficiency measurement, which is performed on a per muon basis.

12. In order to be consistent with the muon trigger efficiency computation the muon track has to be matched at Level 1 and Level 2 with the trigger objects (see Section 3.2)).

The number of selected events is 33,126 and 29,159 for the MUW_W_L2M3_TRK10 and MUW_A_L2M3_TRK10 triggers, respectively. The p_T of the muon, $\not\!\!E_T$ and M_T spectra of these events are presented in Fig. 2.

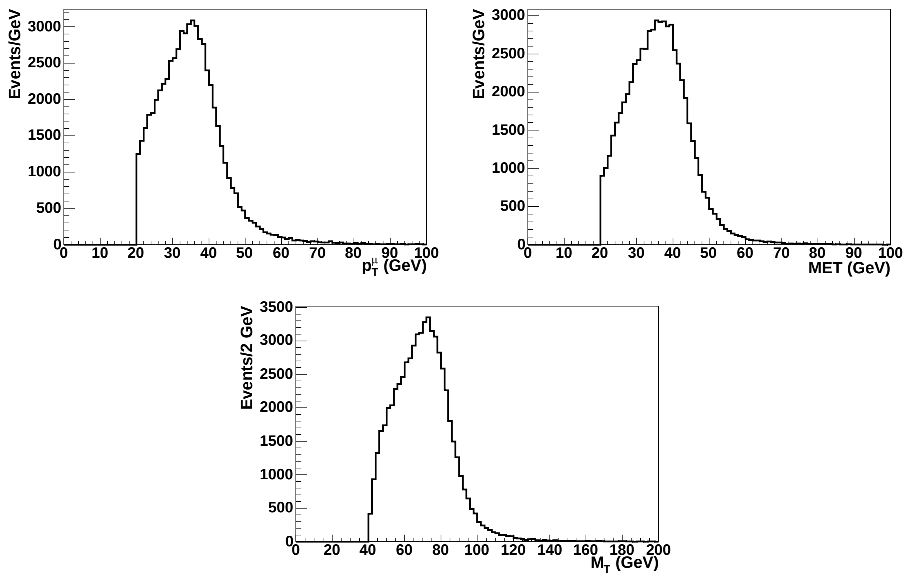

Figure 2: Muon p_T, $\not\!\!E_T$ and M_T distributions in the candidate events.

3 Evaluation of the Efficiencies

The procedure used to measure the tracking, muon identification and trigger efficiencies from data is the same as that used in the $Z \to \mu^+\mu^-$ analysis [6] employing the wzreco and muo_cert [7] packages. This employs the 'tag and probe' method, which utilises the ability to select a clean sample of $Z \to \mu^+\mu^-$ events even if one of the muons has no track associated with it, is not identified in the muon system, or fails to meet the trigger requirements. As the procedure is described is some detail in reference [6] only a brief outline will be given here.

In the text average values are given for the tracking, muon identification and trigger efficiencies. However, in order to properly account for geometrical correlations between these different efficiencies they are measured as a function of position in the detector. These position-dependent efficiencies are simulated in the Monte Carlo used to evaluate the acceptance.

Note the three efficiencies input into the Monte Carlo are

1. The efficiency for a muon to have a reconstructed track

2. The efficiency for a muon to be reconstructed with at least medium quality, satisfy the tight scintillator and loose wire condition at Level-1 and are satisfy the L2M3 condition

at Level-2. These efficiencies are combined together into one 'muon' efficiency to reduce the statistical uncertainty.

3. The efficiency for a muon to have a 10 GeV/c track at Level-3.

The individual muon efficiencies are described separately in order to allow comparisons with these measurements in other analyses. The sample used to evaluate the total 'muon' efficiency is the same one as described in section 3.1.

3.1 Muon ID Efficiency

The medium muon identification efficiency is computed together with the efficiency for a medium muon to be matched with a central track (matching efficiency). It has been shown in reference [6] that it is achievable to select a di-muon sample clean from $b\bar{b}$ background and cosmics by requiring only one of the two muons to fire the single muon trigger and to be reconstructed in the muon chambers. Such a sample will be used in a tag and probe method to estimate muon identification and trigger efficiencies.

The following requirements are used to 'tag' an event as being due to $Z \rightarrow \mu^+\mu^-$:

1. A 'tag' muon is identified of at least medium quality matched to a central track, $p_T >$ 30 GeV/c.

2. The A-layer scintillator timing of the control muon, t_A, has to be: $-7 < t_A < 7\ ns$.

3. A probe track is identified as a $p_T >$ 20 GeV/c central track with $\chi^2/d.o.f < 4$, 8 CFT hits. The $|dca|$ is required to be less than 0.02 cm if the track has SMT hits and less than 0.2 cm otherwise. This track is also required to point within the geometrical acceptance of the muon chamber as defined in Section 2.3.

4. Both muons are required be isolated in the tracker and in the calorimeter.

5. The angular separation of the tracks, ΔR, is required to be greater than 2.0.

6. The acolinearity, defined as $A = \pi - |\phi_1 - \phi_2| + |\theta_1 + \theta_2 - \pi|$, is required to be greater than 0.05.

7. The muons are required to be oppositely charged.

8. The event is required to fire one of the following single muon triggers; MU_W_L2M0_TRK3, MU_W_L2M0_2TRK3, MU_W_L2M3_TRK10, MU_W_L2M5_TRK10, MUW_W_L2M3_TRK10, MUW_W_L2M5_TRK10 or MUW_A_L2M3_TRK10

9. To prevent any bias the control muon has to be associated with the Level 1 and Level 2 muon objects used to trigger the event. The matching requirement between the trigger and offline muon is: $\Delta(\eta_{\mu\ control\ offline}, \eta_{L1}) < 2$, $\Delta(octant_{\mu\ control\ offline}, octant_{L1}) < 2$ and $\Delta R(\mu_{control\ offline}, \mu_{L2}) < 0.95$.

A diagram illustrating the tag and probe method used to obtain muon identification and triggering efficiencies is shown in Fig. 3.

Counting the number of muons in the efficient and inefficient samples an average value for the muon identification efficiency of

$$\epsilon_{medium} = 0.828 \pm 0.004(stat) \tag{2}$$

is found. The muon identification efficiency is introduced into the Monte Carlo as a function of η and ϕ as shown in Fig. 4 as two dimensional plot.

There are a couple of interesting features to note. In the η plot that the muon offline reconstruction efficiency is varying between the different regions of the detector(central/forward). The ϕ plot shows variations due to the gaps between octants in the muon chambers.

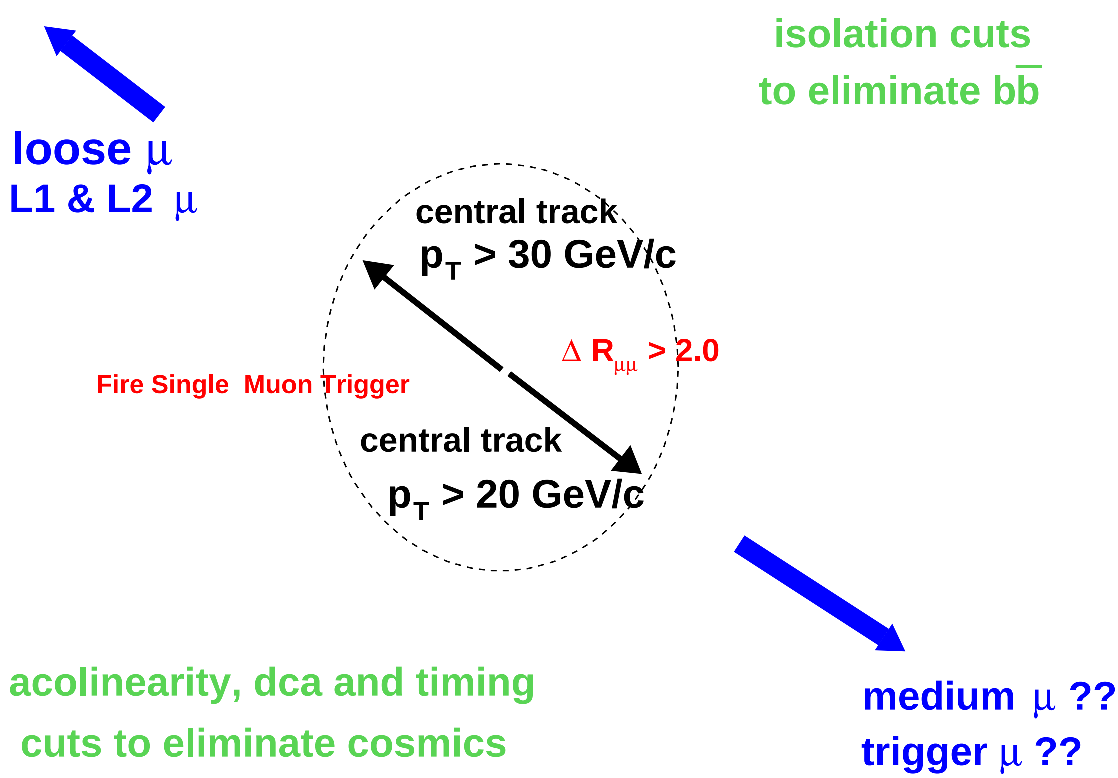

Figure 3: A diagram of the tag and probe method used to obtain the muon identification and trigger efficiencies.

To ensure that there are no significant biases produced using the tag and probe method the efficiencies are measured on a sample of full $Z \rightarrow \mu^+\mu^-$ MC events. The efficiency obtained using the tag and probe method is compared with the 'true' efficiency. This 'true' efficiency is computed by looking if a reconstructed medium muon is found in a $\Delta R < 0.5$ cone around a generated muon. Figure 5 shows that there is a difference of 0.2% between those two efficiencies

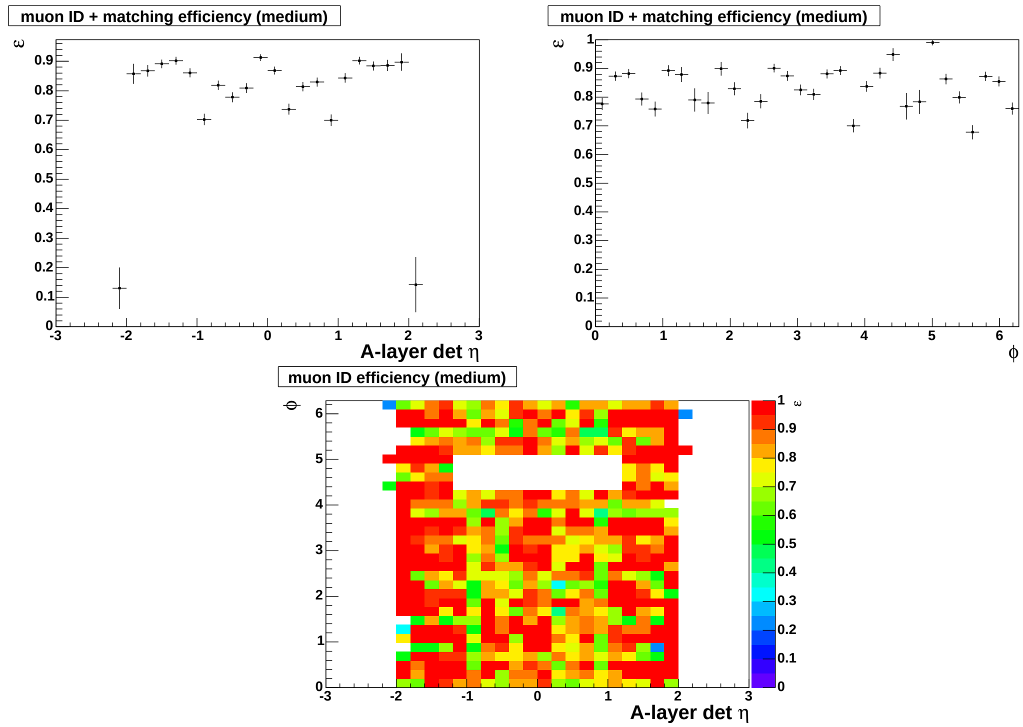

Figure 4: Medium efficiency measured in data using the tag and probe method as a function of the muon detector A-layer η and ϕ in projection and in a two dimensional plot. The errors on the plots are statistical only.

that we will quote as systematic error:

$$\epsilon_{medium} = 0.828 \pm 0.004(stat) \pm 0.002(sys). \tag{3}$$

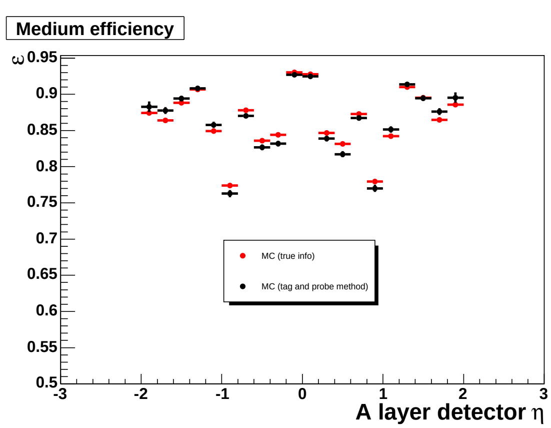

Figure 5: Comparison of the medium muon efficiency in $Z \to \mu^+\mu^-$ Monte Carlo events using the tag and probe method (black) and the true Monte Carlo efficiency (red) as a function of the muon detector A-layer η.

Efficiency of	measured with respect to	MUW_A_L2M3_TRK10	MUW_W_L2M3_TRK10
‘L1 scint’(L1S)	medium muon (M)	0.917 ± 0.003	0.761 ± 0.005
‘L1 wires’ L1W	M/LS	0.974 ± 0.002	0.807 ± 0.005
‘L2M3’	M / L1S / L1W	0.984 ± 0.002	0.984 ± 0.002
‘L3TK’	track	0.792 ± 0.005	0.792 ± 0.005

Table 1: Summary of Trigger efficiencies.

3.2 Muon Trigger Efficiencies

The triggers used in this analysis require tight scintillator hits (the ‘L1scint’ requirement) and loose wire hits at Level-1 (the ‘L1wire’ requirement), for a muon to be identified as of at least medium quality and with p_T greater than 3 GeV/c at Level-2 (the ‘L2M3’ requirement) and for a track with p_T greater than 10 GeV/c to be reconstructed at Level-3 (the ‘L3TK’ requirement). The Level-3 condition will be discussed in the tracking efficiency Section 3.3.

The Level-1 and Level-2 efficiencies are evaluated in the same manner as the medium efficiency in Section 3.1, utilising the same di-muon sample. The only difference is that the probe muon is now required to be identified as of at least medium quality. The efficiency has to be evaluated separately for the two triggers, MUW_W_L2M3_TRK10 and MUW_A_L2M3_TRK10 as the Level-1 condition is different in the two periods.

The trigger efficiencies are summarised in Table 1. Each is obtained by counting the number of muons in the efficient and inefficient samples and all are only averages.

The L1 scint efficiencies are presented in Fig. 6 for both the periods.

The L1 wire efficiencies are shown in Fig. 7 for both the ’wide’ and the ’all’ region of the detector.

The L2M3 efficiency is shown in Fig. 8. Note that this condition is the same for the two triggers and so they can be combined.

As mentioned above the efficiency actually input into the Monte Carlo is an overall ‘muon’ efficiency, including the probability for a muon to be reconstructed and to meet all the Level-1 and Level-2 trigger requirements. This efficiency is plotted for the MUW_W_L2M3_TRK10 and MUW_A_L2M3_TRK10 regions in Fig. 9.

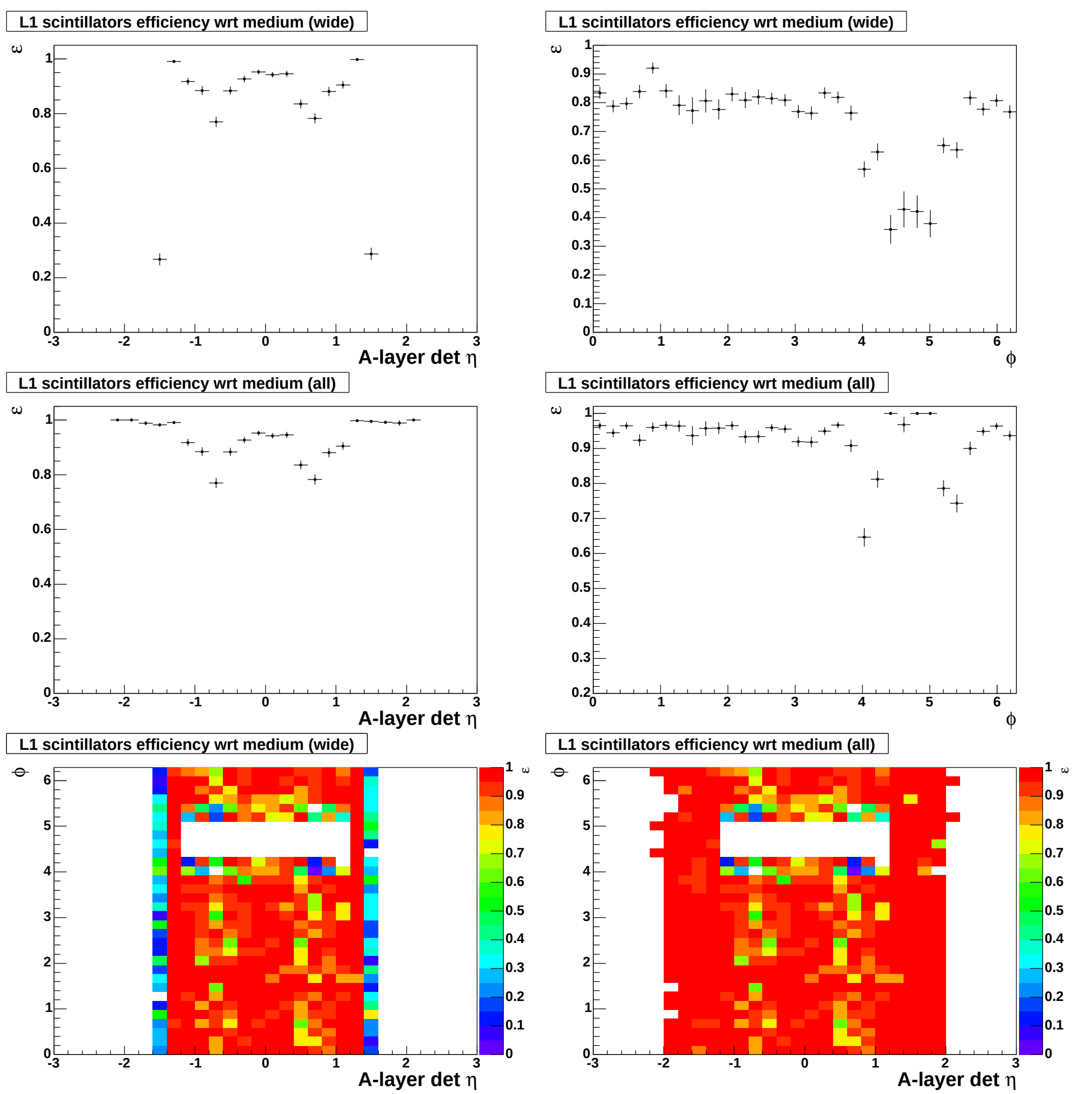

Figure 6: The L1 scint efficiencies with respect to medium muon as a function of the muon detector A-layer η and ϕ for the 'wide' and for the 'all' region of the muon detector.

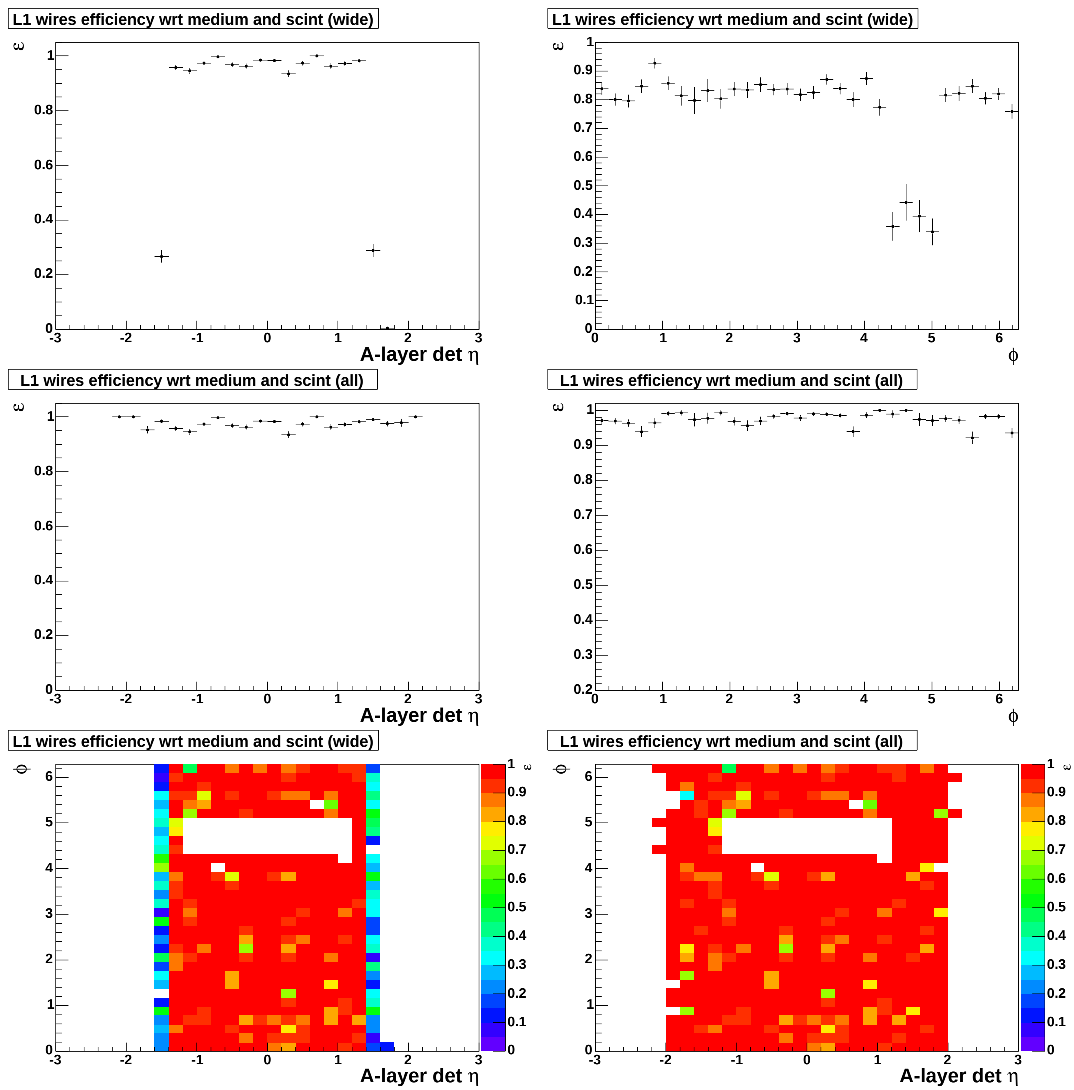

Figure 7: The L1 wire efficiencies with respect to medium muons that have fired the Level 1 scintillator trigger. Those efficiencies are measured in data using the tag and probe method and are plotted as a function of the muon detector A-layer η and ϕ for the 'wide' and for the 'all' regions of the muon trigger.

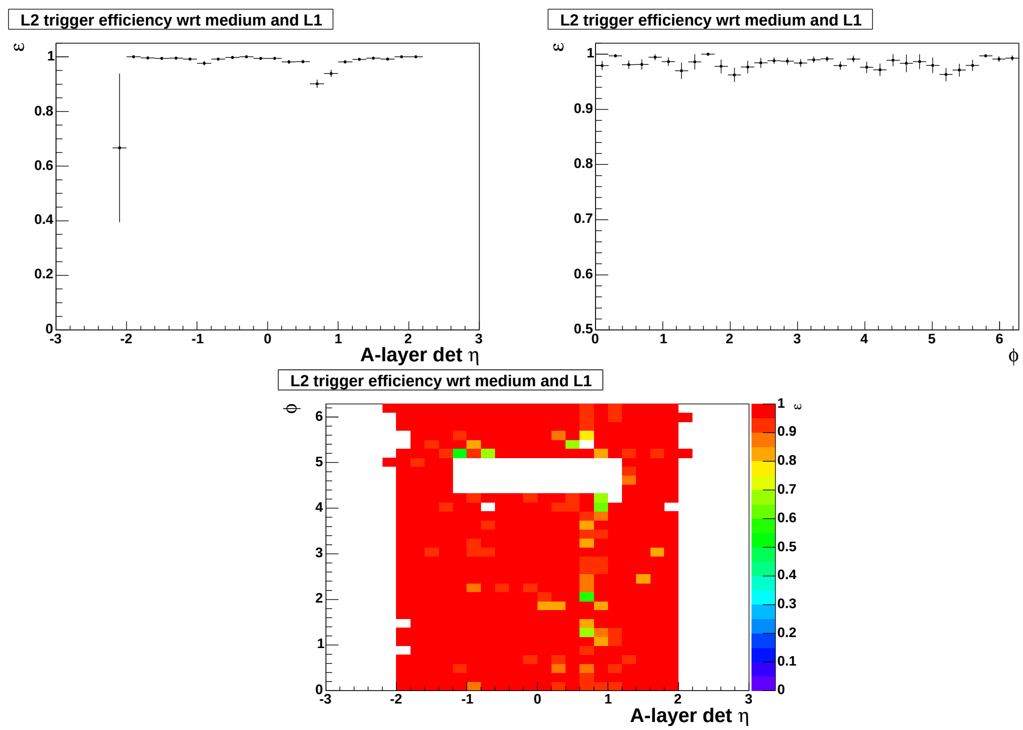

Figure 8: The L2M3 efficiency with respect to offline medium muons that meet the L1scint and L1wire requirements. The efficiency is plotted as a function of the muon detector A-layer η and ϕ.

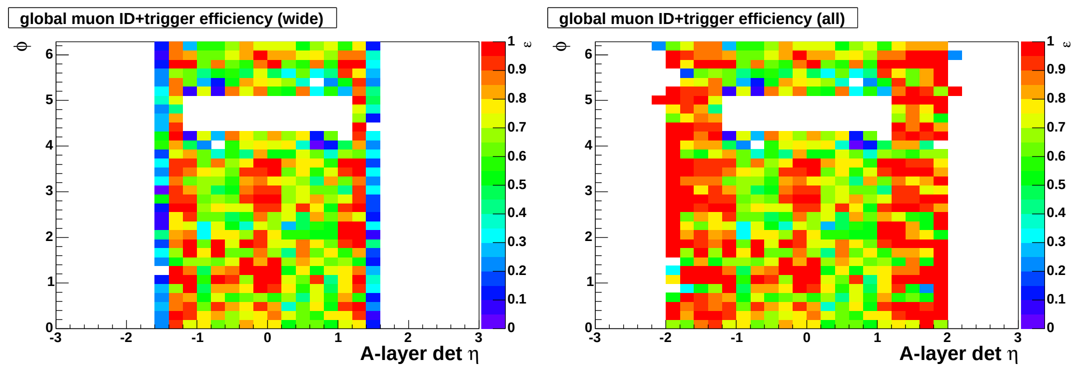

Figure 9: Efficiency for a muon to be reconstructed as medium and to meet the L1scint, L1wire and L2M3 requirements. The efficiency is plotted as a function of the muon detector A-layer η and ϕ. This is plotted separately in the all region (left hand plot) and the wide region (right hand plot).

3.3 Tracking and Level 3 Efficiencies

3.3.1 Tracking Efficiency

It has been shown in reference [6] that it is achievable to select a clean di-muon sample by requiring only one of the two muons to have a reconstructed track. Such a sample will be used in a tag and probe method to measure track reconstruction and trigger efficiencies using the wzreco and muo_cert packages. Note that the track efficiency is the probability that a track is reconstructed, meets the quality requirements as defined in Section 2.3 and has a $|dca| < 0.011$ cm.

The following requirements are used to 'tag' an event as being due to $Z \rightarrow \mu^+\mu^-$:

1. A 'tag' muon is identified of at least loose quality matched to a central track, $p_T >$ 30 GeV/c.
2. The 'tag' muon is required to pass the $W \rightarrow \mu\nu$ isolation cuts.
3. The 'tag' muon is required to have a $|dca|$ less than 0.02 cm.
4. The 'probe' muon is required to be identified in the muon chambers as being of at least loose quality. The loose definition has been modified in order to remove any dependency on the presence of central track matched to the muon.
5. The 'probe' muon is required to be within the geometrical acceptance of the muon chambers as defined in Section 2.3.
6. The angular separation of the two muons, ΔR is required to be greater than 2.0.
7. The time difference between the A layer scintillator times, $|\Delta t|$ is required to be less than 6 ns.
8. To prevent any trigger bias we require that the event fires a di-muon trigger without a track requirement (2MU_A_L2M0, 2MU_A_L2ETAPHI or 2MU_A_L2M0_L3L6,15).

A diagram illustrating the tag and probe method used to obtain the tracking efficiency is shown in Fig. 10.

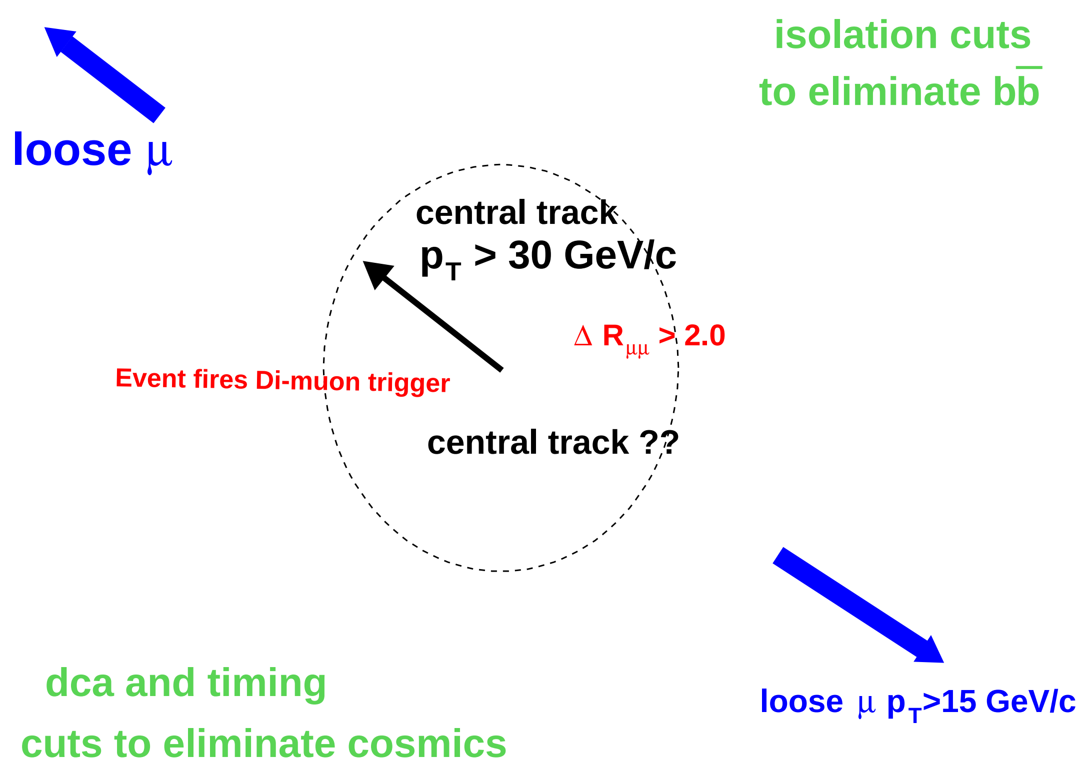

Figure 10: Diagram of the tag and probe method used to obtain the tracking efficiency.

To ensure that there are no significant biases produced using the tag and probe method the efficiencies are measured on a sample of full MC events. The efficiency obtained using the tag and probe method is compared with the 'true' efficiency. This 'true' efficiency is computed by looking if a reconstructed track is found in a $\Delta R < 0.5$ cone around a generated muon. If the efficiency is evaluated only as a function of CFT detector eta[3] then there is a bias of about 3%, as can be seen in Fig. 11.

In order to get rid of this bias, the tracking efficiency has been evaluated in bins of z (position of the track along the beam line). According to the plots in Fig. 12, the bias has mostly disappeared.

As we are now confident that the tag and probe method can be used to provide an unbiased measurement of the tracking efficiency if applied in bins of z, the method has been applied to data (Fig. 13). These efficiencies are then input into the Monte Carlo simulation.

The systematic error on the tracking efficiency is evaluated as the remaining difference between the 'true' and tag and probe efficiency measurements in the full MC (Fig. 12). Both

[3]This is the η of the probe muon central track at the CFT outer radius

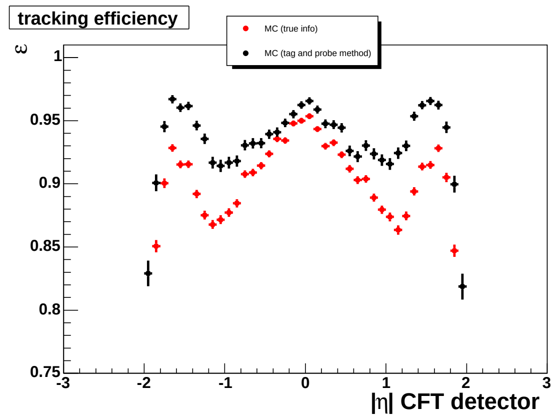

Figure 11: Comparison of the tracking efficiency, with track quality and dca requirements, in $Z \rightarrow \mu^+\mu^-$ Monte Carlo events using the tag and probe method (black) and the true Monte Carlo efficiency (red) averaged over all z as a function of CFT detector η.

efficiencies are input to PMCS and the relative difference in the overall acceptance evaluated to be 0.2%.

Counting the number of muons in the efficient and inefficient samples an average value for the tracking efficiency of

$$\epsilon_{tracking} = 0.834 \pm 0.004(stat) \pm 0.002(sys) \tag{4}$$

is found. The tracking efficiency is introduced into the Monte Carlo as a function of CFT detector η in bins of the z position of the muon track.

3.3.2 Level 3 Tracking Efficiency

The single muon triggers MUW_W_L2M3_TRK10 and MUW_A_L2M3_TRK10 both require a track with $p_T > 10$ GeV/c at Level 3. The efficiency of this condition is computed using the same di-muon sample as for the off-line tracking efficiency in the previous section. The only additional requirement is that of an an offline track associated with the probe muon.

For each of the probe muons, a Level 3 track of $p_T > 10$ GeV/c is required within $\Delta\phi < 0.5$ near the test track. The matching is because the efficiency is measured on a per-muon basis as opposed to a per event basis. This is because it is difficult to measure the probability of another track in the event firing the trigger. The result is shown in Fig. 14.

Counting the number of muons in the efficient and inefficient samples an average value for the Level 3 tracking efficiency of

$$\epsilon_{L3TK} = 0.792 \pm 0.005 \tag{5}$$

is found. The tracking efficiency is introduced into the Monte Carlo as a function of CFT detector η.

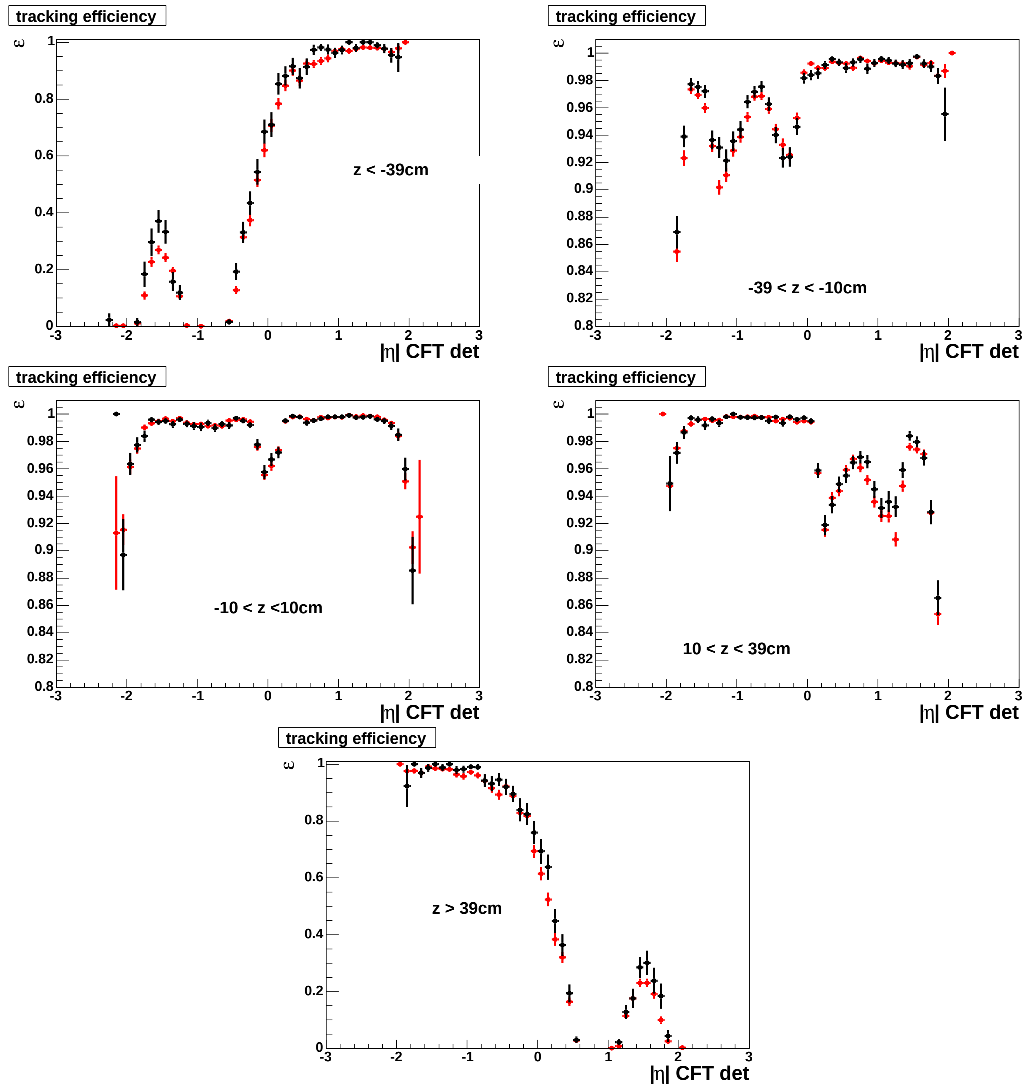

Figure 12: Comparison of the tracking efficiency, with track quality and dca requirements, in $Z \to \mu^+\mu^-$ Monte Carlo events using the tag and probe method (black) and the true Monte Carlo efficiency (red) in bins of z as a function of CFT detector η.

3.4 Time Variation of the Efficiencies

All the measured trigger, muon and track reconstruction efficiencies are averaged over the run period used in the analysis. There are however not constant. The procedure used to determine the uncertainly due to this variation is to evaluate the trigger, medium muon identification and tracking efficiencies as well as the cross section in blocks of runs, each containing about 5 pb^{-1}. For this purpose, only the MUW_W_L2M3_TRK10 trigger has been considered even for the runs when the MUW_A_L2M3_TRK10 trigger is normally used. The combination of those efficiencies is shown in Fig. 15 as a function of the run number. Figure 16 shows the cross section as a function of the run number.

In order to assess an uncertainty due to those variations, the cross section is evaluated in

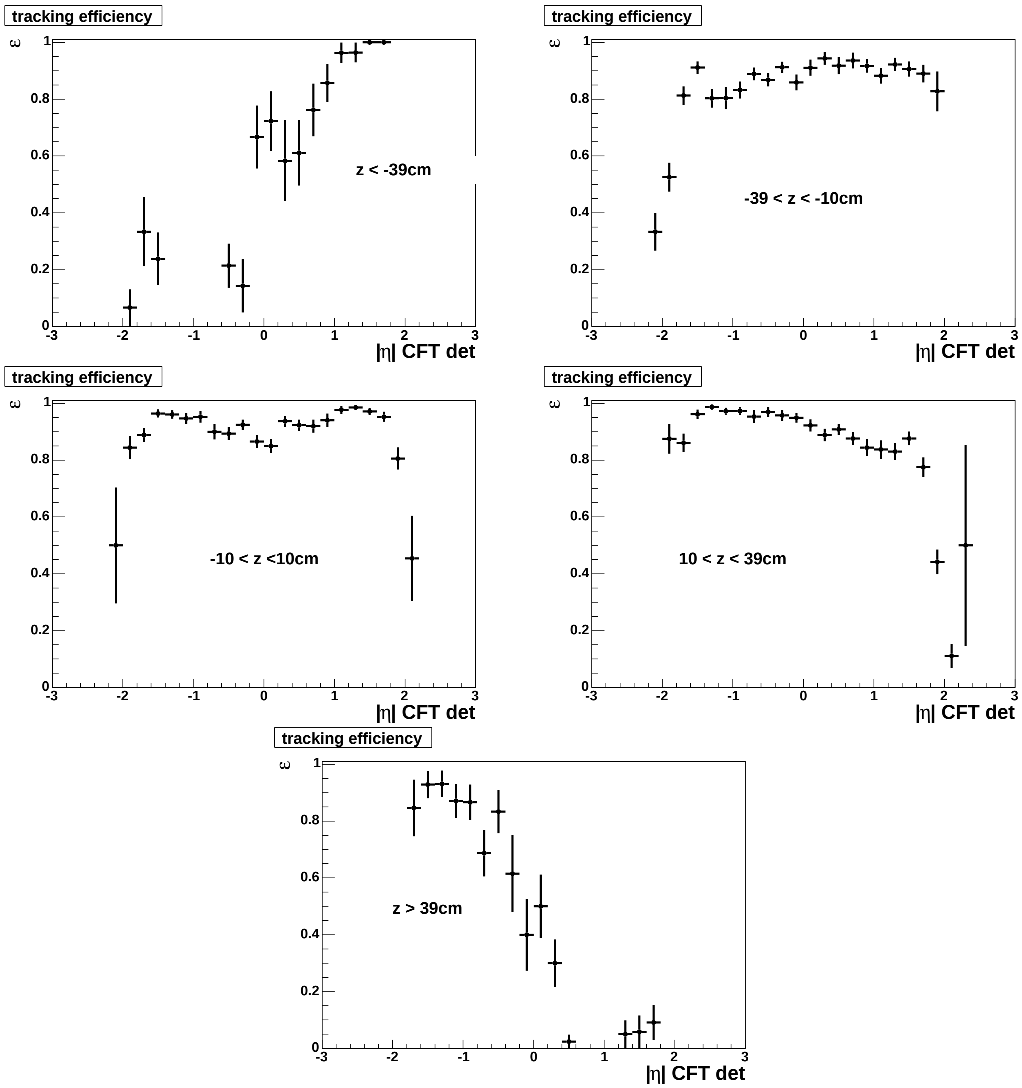

Figure 13: Tracking efficiency, with track quality and dca requirements, measured in data in bins of z as a function of CFT detector η.

each run bin (normalized only with the above efficiencies) and added together, weighted by the luminosity in each bin. This method leads to a difference of 0.6% compared to the evaluation averaging over the whole run range. This difference is quoted as a systematic uncertainty.

3.5 Isolation Efficiency

The isolation requirements are defined in Section 2.3. The justification for the luminosity dependence is discussed in greater detail in the appendix, on page 60. In the Monte Carlo the average value of the luminosity in the $\mathrm{Z} \to \mu^+\mu^-$ data sample, $\mathcal{L} = 0.6 \times 10^{30}\mathrm{cm}^{-2}\mathrm{s}^{-1}$, is used.

The isolation efficiency was determined with $\mathrm{Z} \to \mu^+\mu^-$ data using the tag and probe method. A sample of $\mathrm{Z} \to \mu^+\mu^-$ events is selected, using the same track quality requirements imposed by this analysis. In order to limit $\mathrm{b\bar{b}}$ contamination the control muon is required to

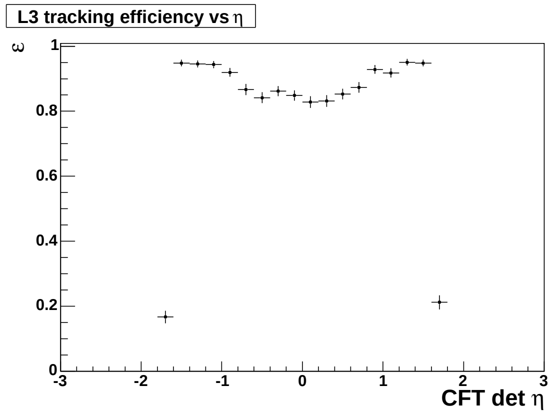

Figure 14: Level 3 tracking efficiency with respect to offline tracks with SMT hit, χ^2 and $|dca|$ requirements measured in data using the tag and probe method as a function of the CFT detector η.

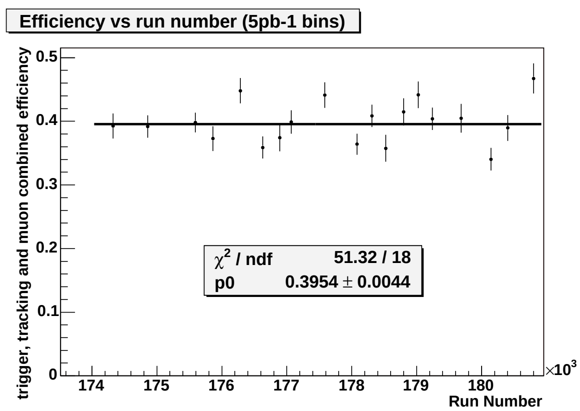

Figure 15: Stability of the combined trigger, tracking and medium muon efficiency as a function of time in blocks of about 5 pb^{-1}.

be isolated. After these events are selected the probe muon is tested to see whether it passes the isolation cuts to give the efficiency. A diagram illustrating the tag and probe method used to obtain the isolation efficiency is shown in Fig. 17.

The tag and probe method is first tested on the full Monte Carlo, to assess any potential biases. A positive bias, due to the isolation requirement on the control muon is found as well as a strong p_T dependency.

3.5.1 Bias of the Tag and Probe Method in the MC

When the isolation efficiency is measured on $Z \to \mu^+\mu^-$ events in the full MC a 1% positive bias is observed as shown in Fig 18(a). This bias is eliminated if the isolation requirement on the tag muon is dropped. Such bias is expected because of correlations between the two muons.

To understand the origin of the bias Figure 18(b) shows the efficiency as a function of the number of reconstructed charged tracks in the $Z \to \mu^+\mu^-$ MC. There are two interesting features

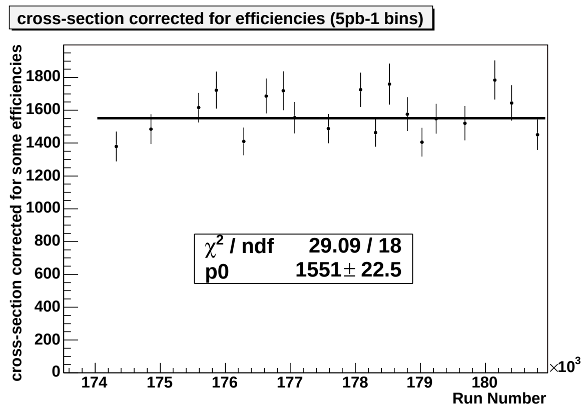

Figure 16: Stability of the cross-section normalized only with the combined trigger, tracking and medium muon efficiency as a function of time in blocks of about 5 pb^{-1}.

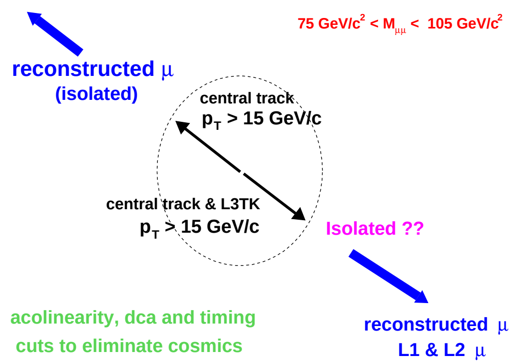

Figure 17: Diagram of the tag and probe method used to obtain the isolation efficiency.

shown in this plot. Firstly the isolation strongly depends on the number of reconstructed tracks. As this quantity is common to the two muons, this creates a strong correlation. Secondly, the tag and probe and Monte Carlo truth information, for any given bin, are in agreement. This demonstrates that this source of correlation is fully responsible for the bias observed in the average efficiency.

3.5.2 p_T Dependency of the Isolation Efficiency in the MC

Figure 18(a) shows the variation of the efficiency as a function of the muon p_T. Figure 19 displays the efficiency as a function of p_T for muons produced in the same direction as the Z boson ($\Delta\Phi(Z,\mu) < \frac{\pi}{2}$) and for muons opposite to the Z ($\Delta\Phi(Z,\mu) > \frac{\pi}{2}$). The p_T dependence disappears for muons along the Z direction.

The p_T dependence is believed to arise from the fact that when a Z boson recoils off a jet, the muon in the same hemisphere as the Z is boosted to a higher p_T. The other muon has lower p_T and is less likely to be isolated as it lies closer to the recoil jet.

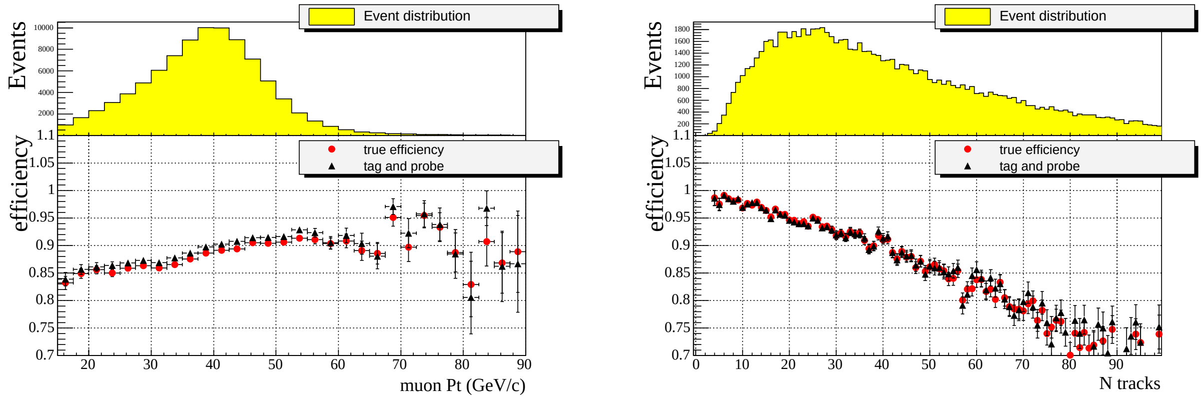

(a) Isolation efficiency as a function of the muon p_T.

(b) Isolation efficiency as a function of the number of charged tracks.

Figure 18: Comparison of isolation efficiency as measured by the tag and probe and Monte Carlo truth methods in a sample of $Z \to \mu^+\mu^-$ full MC events.

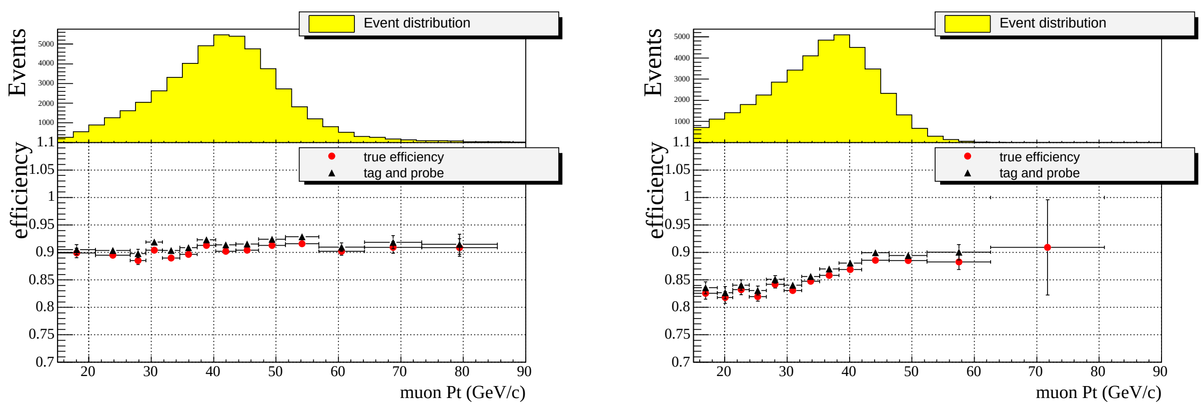

(a) muons collinear to the Z ($\Delta\Phi(Z, \mu) < \frac{\pi}{2}$)

(b) muons opposite to the Z ($\Delta\Phi(Z, \mu) > \frac{\pi}{2}$)

Figure 19: Isolation efficiency as a function of muon p_T in the Z MC.

3.5.3 Parameterisation of the Isolation p_T dependency

To model its variation with p_T, the isolation efficiency is fitted with a S-shape function. The $A + B * \mathrm{Erf}(\frac{p_T - C}{D})$ form is chosen. The parameters are determined at the $Z \to \mu^+\mu^-$ peak using data. The p_T dependence is expected to be different for the $W \to \mu\nu$ events because the W boson has a lower mass than the Z boson. Figure 20 shows that the function obtained in the $Z \to \mu^+\mu^-$ MC is compatible with the one obtained in the $W \to \mu\nu$ MC if the p_T is scaled by the ratio $M_Z/M_W = 91.2/80.4$. Therefore a similar correction is applied to the isolation efficiency measured in data.

According to Fig. 20 the isolation efficiency is lower in the first p_T bins (20 GeV/c $> p_T >$

15 GeV/c) for the W $\rightarrow \mu\nu$ MC when the requirement that M_T is greater than 40 GeV/c^2 is made. Using the approximate formula, $m_T = 2p_T + u_{\parallel}$ (where $u_{\parallel}$ is the projection of the W recoil along the direction of the muon), allows one to understand that an event where the muon has a p_T of 15 GeV/c and a transverse mass above 40 GeV/c^2 is likely to have been produced with a large hadronic recoil. After applying the p_T greater than 20 GeV/c cut, applying the M_T greater than 40 GeV/c^2 cut yields an isolation efficiency that is lower, in the W $\rightarrow \mu\nu$ MC, by 0.2%.

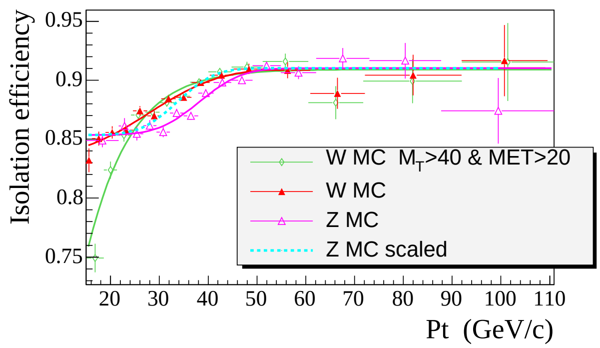

Figure 20: Isolation efficiency as a function of muon p_T in the Z MC and W MC. The fitted function are shown, as well a the function obtained at the Z peak, for which the p_T is scaled by M_Z/M_W.

As a test that this procedure gives a valid measurement of the W $\rightarrow \mu\nu$ isolation efficiency, the efficiency is measured using Z $\rightarrow \mu^+\mu^-$ MC as a function of p_T. This function is scaled down to the W mass, and applied to W $\rightarrow \mu\nu$ MC. When this efficiency is compared to that from W $\rightarrow \mu\nu$ MC (with the M_T cut applied) the values differed by less than 0.1%, which is considered to be negligible as a systematic.

3.5.4 Measurement of the Isolation Efficiency using Data

The isolation efficiency used in the analysis is taken from Z $\rightarrow \mu^+\mu^-$ data using the tag and probe method. Fig. 21(a) shows the dependence of the isolation efficiency on the number of tracks in data, which can be compared to the same plot in the MC in Fig. 18(b). The behaviour exhibited in these plots is similar and so we conclude there will be a positive bias, of $\simeq$ 1%, present in the tag and probe efficiency measurement in data.

Examination of Fig. 21(b) shows that there is dependency of the efficiency with η. The average over the “all” region is will be different than over the “wide”region, so the measurement is made independently in the two samples.

An event is only included in the efficiency measurement in the MUW_W_L2M3_TRK10 period if the test muon fired the MUW_W_L2M3_TRK10 trigger, and similarly events used to evaluate the efficiency in the MUW_A_L2M3_TRK10 period are required to fire the MUW_A_L2M3_TRK10 trigger.

The isolation efficiencies for the MUW_A_L2M3_TRK10 and MUW_W_L2M3_TRK10 periods, with and without the isolation requirement on the control muon, are summarised in Table 2. The first column is the isolation efficiency if no isolation requirement is made on

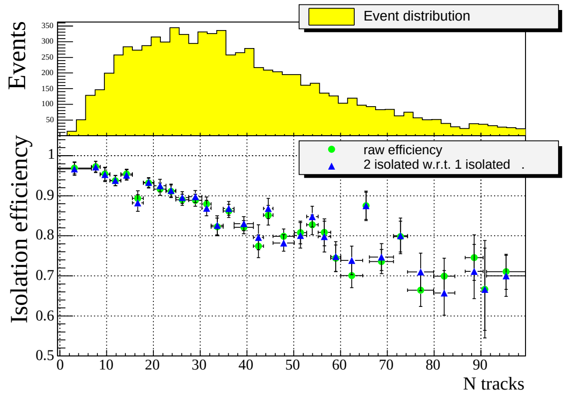

(a) Isolation efficiency as a function of the number of charged tracks.

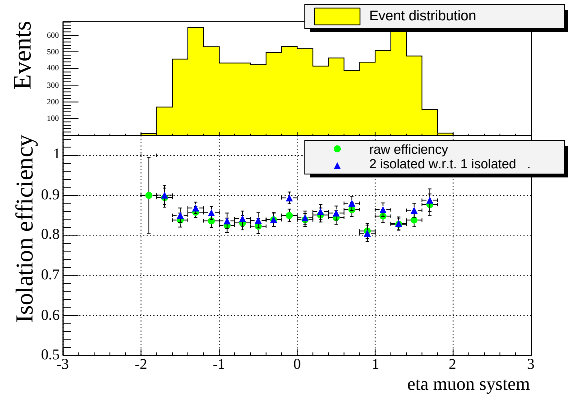

(b) Isolation efficiency as a function of muon detector eta.

Figure 21: Isolation efficiency measured in $Z \rightarrow \mu^+\mu^-$ data using the tag and probe method. No isolation requirements are made on the control muon here.

period	ϵ_{iso} (no iso)	ϵ_{iso} (iso)	Final
MUW_W_L2M3_TRK10	$85.3\% \pm 0.5\%$	$86.1\% \pm 0.5\%$	$85.7\% \pm 0.6\%$(stat) $\pm 0.5\%$(syst)
MUW_A_L2M3_TRK10	$83.7\% \pm 0.6\%$	$85.6\% \pm 0.6\%$	$84.6\% \pm 0.6\%$(stat) $\pm 0.5\%$(syst)

Table 2: Isolation efficiencies obtained at the $Z \rightarrow \mu^+\mu^-$ peak.

the control muon. This is expected to be a lower bound because of $\mathrm{b}\bar{\mathrm{b}}$ contamination of the efficiency sample. The second column is the efficiency obtained if the control muon is required to be isolated, this is expected to be an upper bound due to the bias discovered in the MC.

For MUW_A_L2M3_TRK10, the difference between the upper and lower bound is 1.9%. Assuming a bias of 1% a small reduction in the efficiency attributed to $b\bar{b}$ contamination of 0.9% can be infered. The difference amounts to 0.8% for the MUW_W_L2M3_TRK10 events, so the $b\bar{b}$ contamination seems to be negligible.

As the exact amount of bias on the data is not known, it is impossible to disentangle it from the effect due to $\mathrm{b}\bar{\mathrm{b}}$ contamination. The efficiency is estimated by averaging the figures from the two methods and quoting half the expected bias as a systematic error. This covers a reasonable amount of the effect due to $\mathrm{b}\bar{\mathrm{b}}$ contamination and a possible deviation of the bias from the expected 1%. Therefore the figures for the isolation efficiency, at the $Z \rightarrow \mu^+\mu^-$ peak are:

$$\text{for MUW\_W\_L2M3\_TRK10 } \epsilon = 85.7\% \pm 0.6\%(\text{stat}) \pm 0.5\%(\text{syst})$$
$$\text{for MUW\_A\_L2M3\_TRK10 } \epsilon = 84.6\% \pm 0.6\%(\text{stat}) \pm 0.5\%(\text{syst}).$$

To utilise this efficiency for the $W \rightarrow \mu\nu$ analysis, one more step is needed. The isolation efficiencies as fitted functions of (scaled) p_T, as shown in Figures (22(a)) and (22(b)), and added into the Monte Carlo. When the isolation efficiency is computed for the Monte Carlo simulation used to evaluate the acceptance the efficiencies are found to be:

$$\epsilon = 84.7\% \pm 0.6\%(\text{stat}) \pm 0.5\%(\text{syst}) \text{ for MUW\_W\_L2M3\_TRK10}$$
$$\epsilon = 84.3\% \pm 0.6\%(\text{stat}) \pm 0.5\%(\text{syst}) \text{ for MUW\_A\_L2M3\_TRK10.}$$

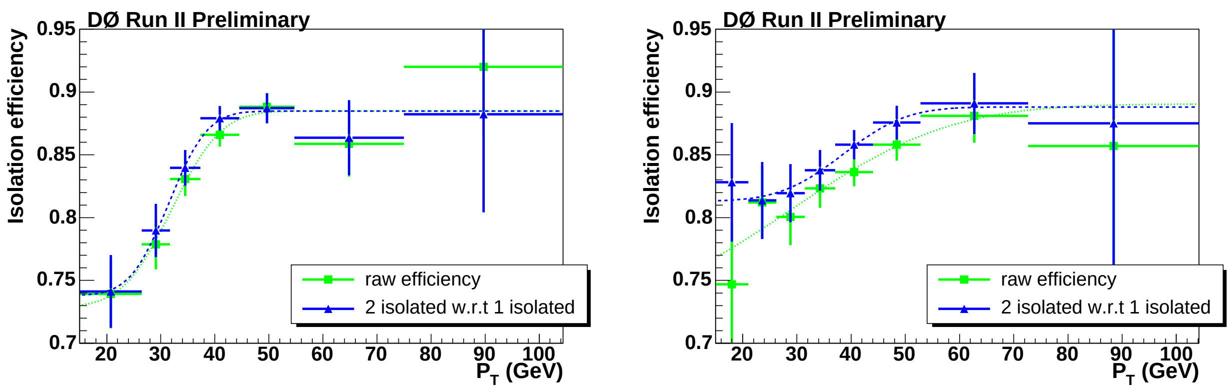

(a) Isolation efficiency for MUW_W_L2M3_TRK10 events.

(b) Isolation efficiency for MUW_A_L2M3_TRK10 events.

Figure 22: Isolation efficiency with and without the isolation requirement on the control muon.

3.6 Z $\rightarrow \mu^+\mu^-$ Veto Cut Efficiency

To remove Z $\rightarrow \mu^+\mu^-$ events contaminating the W $\rightarrow \mu\nu$ sample events are removed if an extra medium muon or an extra high p_T track is present in the event.

3.6.1 Choice of the Cuts

The fraction of Z $\rightarrow \mu^+\mu^-$ events remaining in the candidate events is evaluated using the fast Monte Carlo simulation as described in Section 5.1. Most Z $\rightarrow \mu^+\mu^-$ events that pass the selection cuts possess a muon too far forward to be within the acceptance of the detector and hence are indistinguishable from a W $\rightarrow \mu\nu$ events.

To obtain an estimate of the Z $\rightarrow \mu^+\mu^-$ contamination it is essential that both the efficiency and the object multiplicity are well reproduced in the Monte Carlo. We use PMCS for the evaluation of the Z $\rightarrow \mu^+\mu^-$ contamination as PMCS has the appropriate efficiencies per construction. As PMCS doesn't model the mis-reconstructed low quality objects or in-flight decays, we have to impose quality criteria on the veto objects so that the veto cuts can be simulated by PMCS.

The track based Z $\rightarrow \mu^+\mu^-$ veto is designed to removes Z $\rightarrow \mu^+\mu^-$ and cosmic ray events when one muon is not reconstructed in the muon system but is observed in the central tracker.

Because the two muons are mostly produced back to back in ϕ and to avoid picking a veto track which is not due to $Z \rightarrow \mu^+\mu^-$ we require the veto track to be opposite in ϕ candidate muon, i.e.: $\Delta(\phi_W, \phi_{track\ veto}) > 2.1$.

To avoid contamination from mis-measured tracks, the veto track has to fulfill the same track requirements made in the event $W \rightarrow \mu\nu$ selection:

1. p_T must be greater than 20 GeV/c.

2. χ^2/d.o.f.< 3.3.

3. Track must have at least one SMT hit.

4. $|dca| < 110\ \mu$m, where dca is the distance of closest approach of the muon track to the beam position in the x-y plane.

In order to have a well defined efficiency the muon detector η of the veto track has to be less than 2.

The muon based veto allows us to remove $Z \rightarrow \mu^+\mu^-$ events when one muon falls outside of the tracking acceptance or is not reconstructed in the central tracker. The Muon veto requires that there is no other medium muon with $|nseg| = 3$ in the event. For a muon to have $|nseg| = 3$ requires it to have hits both within and without the toroid [8]. To avoid vetoing on mis-reconstructed fake muons around the candidate muon, we require the veto muon to be separated from the candidate muon: $\Delta(\phi_W, \phi_{muon\ veto}) > 0.1$.

3.6.2 Efficiency Computation

The efficiency of the veto requirement is evaluated, along with the rest of the acceptance, using PMCS. As a cross check the efficiency of the veto is evaluated using $Z \rightarrow \mu^+\mu^-$ data and $Z \rightarrow \mu^+\mu^-$ and $W \rightarrow \mu\nu$ full MC samples.

The method used to compute the efficiency in data starts by selecting a clean sample of $Z \rightarrow \mu^+\mu^-$ events. One muon is required to satisfy all the $W \rightarrow \mu\nu$ event selection requirements (cf Section 2.3). The other muon is required to have high p_T pass cuts designed to veto against cosmic rays, be identified as at least medium quality, be matched to a central track, be isolated in the calorimeter and have the opposite sign charge to the first muon. This second muon is then removed from the event to mimic a W event.

We then count the number of those "fake W" events that are removed by the veto criteria to estimate the veto efficiency. To avoid any bias coming from the muon activity around the removed muon, we don't take into account muons that are in a cone $\Delta R < 0.5$ around the removed muon. The track veto efficiency and the combined track and muon veto efficiency are shown in Fig. 23 as a function of the $\Delta\phi$ cut between the muon track from W decay and the veto track. The veto efficiency is then found to be: $\epsilon_{veto} = 99.51 \pm 0.09$(stat)% for $\Delta(\phi_W, \phi_{track\ veto}) > 2.1$.

To validate the computation of the efficiency using $Z \rightarrow \mu^+\mu^-$ events, we use events simulated using the full Monte Carlo and apply the method used in data. Using this method the efficiency is found to be $\epsilon_{MC\ Z} = 99.09 \pm 0.05$(stat)%. If we use full Monte Carlo $W \rightarrow \mu\nu$ events (without removing any muons in that case), the efficiency is evaluated to be $\epsilon_{MC\ W} = 99.03 \pm 0.06$(stat)%. The two estimates agree well which shows that we can use

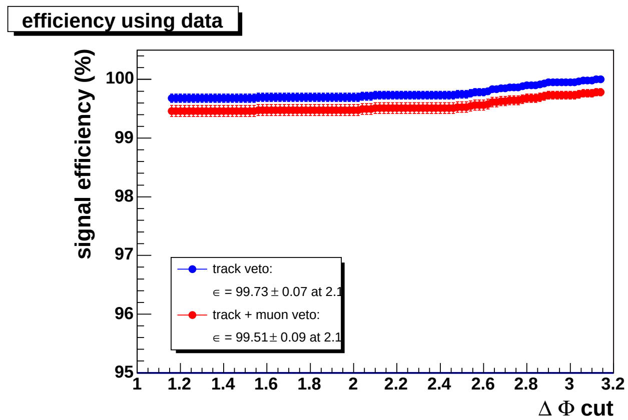

Figure 23: Track veto efficiency and combined track and muon veto efficiency as a function of the $\Delta\phi$ cut between the muon track from W decay and the veto track measured using Z $\rightarrow \mu^+\mu^-$ data. The chosen cut is $\Delta(\phi_W, \phi_{track\ veto}) > 2.1$.

Z $\rightarrow \mu^+\mu^-$ events which is encouraging. Those Monte Carlo estimates are lower than that obtained using data. This is to be expected since both the tracking and muon ID efficiencies are higher in Monte Carlo than in data.

Using the muon removal method with PMCS Z $\rightarrow \mu^+\mu^-$ events the efficiency is found to be $\epsilon_{PMCS\ Z} = 99.54 \pm 0.05$(stat)%. With PMCS W $\rightarrow \mu\nu$ events the efficiency is found to be $\epsilon_{PMCS\ W} = 99.48 \pm 0.05\%(stat)$.

However those PMCS efficiencies are computed using the medium muon efficiency (which is the criterion used for the candidate muon), not the medium $|nseg| = 3$ criterion. The efficiency of medium + $|nseg| = 3$ muons is: $\epsilon_{medium+nseg} = 80.24 \pm 0.40\%$ which is 3% smaller than the medium efficiency alone. As the loss of efficiency due to the medium muon veto with respect to the track veto is 0.22% (cf. Fig. 23), the error on the veto efficiency due to the muon input wrong efficiency in PMCS is around 0.01%. The largest difference between the PMCS and data is used as an estimate of the systematic error; producing

$$\epsilon_{veto} = 99.51\ \pm 0.1\ (\text{stat})\ \pm 0.1\ (\text{syst})\%. \tag{6}$$

The cross section is measured with the track veto removed and the muon veto removed in Section 7. The variation in the cross section when this is done cannot be trivially exchanged and so these differences are quoted as a 1.2% systematic.

4 Description of the Monte Carlo Simulation, PMCS

The acceptance, and the 'electroweak' backgrounds are evaluated using a fast Monte Carlo simulation, PMCS. Firstly events are generated using the PYTHIA event generator [13] employing the CTEQ6.1 PDF set [14]. The Tune 'A' model of the underlying event has been employed as well as CDF's tuning of the Z p_T [15]. The effect of detector resolution on these events is modelled using PMCS.

PMCS (Parameterised Monte Carlo Simulation) is based on parameterised physics processes and reconstruction, making it much faster than a full reconstruction. It works by simulating the smearing effects of the DØ detector on high level physics objects, such as jets and muons. This is done using a selection of parameters tuned to the data taken from the DØ detector. The following sections describe how the p_T and $\not\!\!E_{\mathrm{T}}$ resolutions are modelled as well as a brief description of how the efficiencies are handled. The sources of systematic uncertainty from sources such as the modelling of the luminous region and from choice of PDF are described.

4.1 PMCS tuning

The effects of detector resolution on the p_T measurement is simulated as described in equation (7) using three (variable) parameters, denoted A, B and C. Firstly the generated p_T is smeared using a gaussian with a width given by equation (7). The resultant, smeared, p_T is then scaled using equation 8 [11].

$$\frac{\sigma_{1/p_T}}{1/p_T} = \sqrt{A^2 \frac{{p_T}^2}{L^4} + \frac{B^2}{Lsin(\theta)}} \tag{7}$$

$$p_T(final) = C.p_T(smear) \tag{8}$$

A parameterises the effect on the p_T resolution caused by the measurement error of individual hits in the tracker. This increases proportional to p_T and inversely to the normalised tracking bending lever arm (L). B parameterises the effect of multiple scattering on the resolution. C parameterise the imperfect description of the magnetic field in the reconstruction process and also the energy loss caused by passing through material.

The parameterisation is the same as that described in reference [11], but the values of the parameters have to be re-tuned to reflect the more stringent requirements made on the track quality by this analysis. It is assumed that the effect of multiple scattering on the p_T resolution is insensitive to the track quality requirements and so B is not changed. The values of parameters A and C are tuned using a sample of $\mathrm{Z} \rightarrow \mu^+\mu^-$ data, where the track quality cuts from the $\mathrm{W} \rightarrow \mu\nu$ analysis have been applied.

Firstly A is roughly tuned "by eye" to be 0.00225, then C roughly tuned to be 0.992. Then A is tuned by minimising the χ^2 of a data-MC comparison of the $\mathrm{Z} \rightarrow \mu^+\mu^-$ peak to be 0.00232 $\pm$ 0.00010. Finally C is tuned by minimising the χ^2 of a data-MC comparison of the $\mathrm{Z} \rightarrow \mu^+\mu^-$ peak to be 0.995 $\pm$ 0.003. Figure 24 illustrates the tuning process.

The parameterisation of the missing energy resolution is the same as that used in the $\mathrm{W} \rightarrow \mathrm{e}\nu$ analysis (see reference [12] for details), with one exception. This exception is that an additional term has had to be added to model the energy deposited by the muon in the calorimeter.

In the $\mathrm{W} \rightarrow \mathrm{e}\nu$ analysis the smeared $\not\!\!E_{\mathrm{T}}$ is evaluated using the recoil jet, the smeared lepton, the generated $\not\!\!E_{\mathrm{T}}$ and a term to simulate the effect of the underlying event.

The E_{T} of the recoil jet is smeared using the following parameterisation,

$$E_{\mathrm{T}}'_{recoil} = E_{\mathrm{T}recoil} * \alpha \tag{9}$$

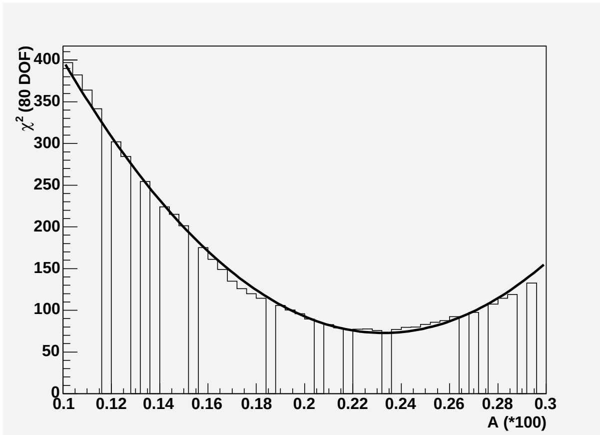

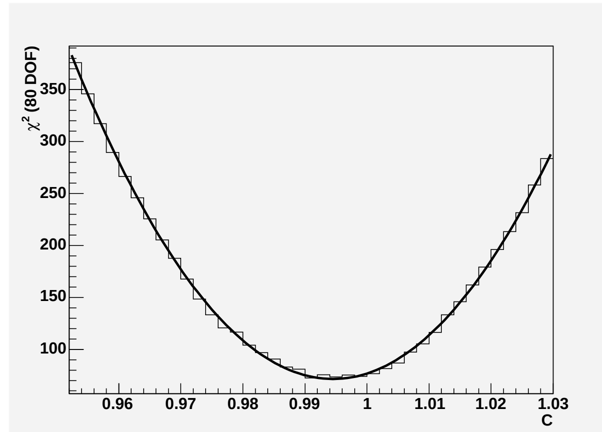

Figure 24: Value of χ^2 in comparison of $Z \to \mu^+\mu^-$ data, using the track quality cuts from the $W \to \mu\nu$ analysis, and PMCS. In the left hand plot parameter A is varied and in the right hand plot parameter C is varied.

Parameter	Value with Uncertainty
α	0.60 ± 0.02
S	0.80 ± 0.20 GeV$^{\frac{1}{4}}$
C	0.05 ± 0.01
U	3.02 ± 0.04 GeV

Table 3: Summary of parameters used to smear $\not\!\!E_{\mathrm{T}}$.

$$\frac{\sigma_{E_{\mathrm{T}}{}'_{recoil}}}{E_{\mathrm{T}}{}'_{recoil}} = \sqrt{C^2 + \frac{S^2}{\sqrt{E_{\mathrm{T}}{}'_{recoil}}}} \tag{10}$$

$$E_{\mathrm{T}recoil}(smear) = E_{\mathrm{T}}{}'_{recoil} + x * \sigma_{E_{\mathrm{T}}{}'_{recoil}} \tag{11}$$

where α is the hadronic energy scale[4], C and S are the constant and sampling terms for the hadronic calorimeter, and x is a random number with a gaussian distribution with mean 0 and RMS 1.

The underlying event is simulated using a vector with random direction and a magnitude randomly distributed according to a gaussian of mean zero and width U.

All the parameters are taken from reference [12] and are summarised in Table 3.

The other $\not\!\!E_{\mathrm{T}}$ component is the addition of the energy deposited by the muon as it passes through the calorimeter. This uses a simplified model of the calorimeter constructed by D. Hedin in Run I [5]. This models the energy that a muon is expected to deposit in the calorimeter. To get the transverse component of this the energy is divided by $cosh(\eta)$. The quantity is then multiplied by a tunable parameter k, which represents a kind of 'MIP' energy scale.

[4] α is denoted the hadronic energy scale to keep consistency with the nomenclature used in reference [12]. However it is really an energy scale for the 'whole calorimeter'. Similarly C and S are the sampling and constant terms for the whole calorimeter.

[5] No reference has been determined for this as yet. The code is available in MuoCandidate.

To determine the value of k, we use the distribution of the W recoil along the direction of the muon, $u_{\|}$. This variable integrates calorimeter quantities projected onto the direction of the muon and is therefore the most sensitive variable to any change in the MIP scale factor. The value of k is found to be 0.78 ± 0.02 by optimising the agreement between data and PMCS in the distribution of $u_{\|}$ as shown in Fig. 25(a). To assess the systematic error, the optimisation of k is also performed, using the $\not{E}_{\mathrm{T}}$ distribution. This yields a slightly different value of 0.53 ± 0.03, as shown in Fig. 25(b). The difference $0.78 - 0.53 = 0.25$ is taken as a systematic error and we quote the value obtained using $u_{\|}$ as the central value : $k = 0.78 \pm 0.25$. The 0.25 uncertainty on k can be propagated to the overall W $\rightarrow \mu\nu$ acceptance, giving a relative error of 0.5%.

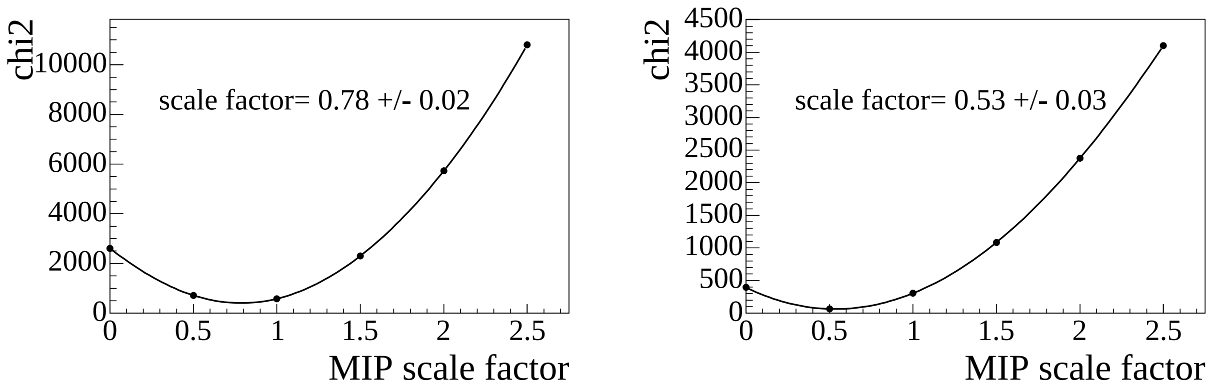

(a) χ^2 using the distribution of $u_{\|}$.

(b) χ^2 using the distribution of $\not{E}_{\mathrm{T}}$.

Figure 25: χ^2 versus value of k in data-PMCS comparison of W $\rightarrow \mu\nu$ data.

The smeared $\not{E}_{\mathrm{T}}$ is then calculated using the following vector sum

$$\underline{\not{E}_{\mathrm{T}}} = -\underline{p_{T\mu}} - \underline{E_{\mathrm{T}recoil}}(smear) - \underline{E_{\mathrm{T}U.E.}} - \underline{E_{\mathrm{T}M.I.P.}} \tag{12}$$

where $\underline{p_{T\mu}}$ is the smeared p_T of the muon, $\underline{E_{\mathrm{T}recoil}}$(smear) is the smeared E_{T} of the recoil jet, $\underline{E_{\mathrm{T}U.E.}}$ is the smeared E_{T} of the underlying event and $\underline{E_{\mathrm{T}M.I.P.}}$ is the transverse energy deposited by the muon in the calorimeter.

4.2 Tuning of the Vertex z Distribution

Interactions inside the DØ detector have an approximately Gaussian distribution as a function of z. This analysis is sensitive to this distribution because of the strong dependency of the tracking efficiency as a function of z. For instance changing the width of Gaussian distribution used to generate events from the default value of 25 cm to the 28 cm used by the Z $\rightarrow e^+e^-$ and W $\rightarrow$ eν analyses results in a 4% change in the acceptance. Shifting the center of this gaussian from 0 to 2 cm yields a reduction of 0.2% in acceptance.

Both the width of the Gaussian, σ, and the offset of the Gaussian from 0, z_{off}, are tuned to optimise the agreement between data and Monte Carlo. This is done using a re-weighting

Sample	'wide' region		'all' region	
range for χ^2 computation	whole range	core	whole range	core
best width (cm)	26.7 ± 0.2	26.4 ± 0.3	27.2 ± 0.2	26.5 ± 0.4
best offset(cm)	1.8 ± 0.2	1.5 ± 0.2	1.6 ± 0.2	1.5 ± 0.3

Table 4: Computation of the vertex z distribution parameters for four cases. The errors quoted are statistical.

technique; events generated with an offset z_{MC} and a width σ_{MC} are weighted by the function

$$\frac{\sigma_{MC}}{\sigma_{test}} \times \frac{\exp\left(-\frac{(z-z_{test})^2}{2\sigma_{test}^2}\right)}{\exp\left(-\frac{(z-z_{MC})^2}{2\sigma_{MC}^2}\right)}$$

where σ_{test} and z_{test} are the tested distribution width and offset respectively. The χ^2 of the difference between data and MC of the z distribution (see Fig. 40) is computed. The χ^2 minimization yields the plots shown in Fig. 26. These plots are produced using data from the MUW_A_L2M3_TRK10 period and by restricting the χ^2 computation to the core of the distributions, i.e. the bins in the range $-39 < z < 39$ cm.

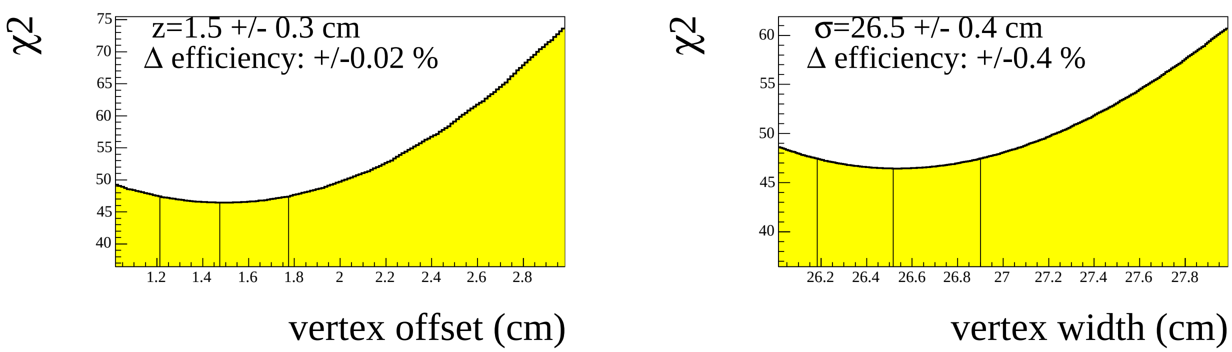

(a) determination of vertex offset

(b) determination of vertex width

Figure 26: Determination of the vertex parameters. The errors quoted here are statistical.

The χ^2 minimization is performed in four cases, for both the MUW_W_L2M3_TRK10 or MUW_A_L2M3_TRK10 periods and either computing the χ^2 in the whole range of z or restricting to the core $-39 < z < 39$ cm. The results are summarized in Table 4.

The fit for the core of the distribution agrees quite well for MUW_A_L2M3_TRK10 and MUW_W_L2M3_TRK10 events. The fit in the whole range give higher widths and is probably an overestimation, given the coarseness of the binning as a function of z used for the tracking efficiency calculation. The Monte Carlo events used to evaluate the acceptance is generated using the value obtained with the core distribution. Half of the spread of the results of Table 4 is taken as systematic error:

$$\sigma = 26.5 \ \pm 0.4 \text{ (sys)} \ \pm 0.4\text{(stat) cm}$$
$$z_{off} = 1.5 \ \pm 0.2 \text{ (sys)} \ \pm 0.2\text{(stat) cm.}$$

Propagated to the W $\rightarrow \mu\nu$ acceptance, the uncertainty on the z offset is negligible ($\simeq$ 0.03%) while for the width we obtain 0.8% and 0.6% for the MUW_W_L2M3_TRK10 and MUW_A_L2M3_TRK10 samples, respectively.

4.3 Signal Acceptance

The acceptance is defined to be the product of the geometric and kinematic acceptances with the tracking, muon identification and triggering efficiencies. The tracking, muon identification and trigger efficiencies are measured in data, as described in section 3. Each efficiency is then introduced in the Monte Carlo by accepting a condition (eg has track, identified as muon, etc) with probability as function of detector position.

The acceptance is defined to be the ratio between the number of events accepted to the number of events generated. Events are selected if they pass the event selection as described in section 2. The acceptances of the two periods, evaluated using a sample of 500k W $\rightarrow \mu\nu$ events, were found to be

$$\epsilon = 22.37\% \text{ for MUW\_W\_L2M3\_TRK10 trigger}$$
$$\epsilon = 25.59\% \text{ for MUW\_A\_L2M3\_TRK10 trigger}$$

respectively. The statistical error on these numbers is negligible ($\simeq 0.05\%$). The systematic errors are addressed in the following sections.

4.4 PDF Uncertainty

The CTEQ6.1 PDF fit comes with 40 'error' sets which are associated with the uncertainty on each of the 20 parameters in the global PDF fit [14]. Each parameter is increased and decreased in such a way to increase the χ^2 of the global fit by 'one sigma' producing two 'error' PDF sets. The uncertainty due to choice of PDF is then a sum of the uncertainty due to these parameters.

The following sum is used to evaluate asymmetric errors

$$\Delta X_{\pm} = \sum_{i=1}^{20} (X^{\pm} - X_0)^{\frac{1}{2}}. \tag{13}$$

For each pair of PDF sets the acceptance is evaluated and positive differences are added to the positive uncertainty and negative ones to the negative uncertainty. If both are positive or negative then they are averaged and added to the appropriate uncertainty (The TevEWWG prescription). If the DØ prescription is used the uncertainties increase by 0.1%. The TevEWWG is retained for ease of comparison with CDF.

The uncertainty in the acceptance due to the choice of PDF is found to be +1.3%-1.5% and +1.3%-1.1% on the MUW_W_L2M3_TRK10 and MUW_A_L2M3_TRK10 periods using this method. For the ease of combining with the other uncertainties these numbers are symmeterised to be ± 1.4% and ± 1.2% in the MUW_W_L2M3_TRK10 and MUW_A_L2M3_TRK10 periods respectively.

Source of Uncertainty	'all' region	'wide' region	$\sqrt{(covariance)}$
PDF	1.4%	1.2%	1.2%
Modelling of W p_T	0.2%	0.2%	0.2%
Statistical Uncertainty ($Z \rightarrow \mu^+\mu^-$ sample)	0.9%	0.9%	0.9%
Variation with time of the Efficiencies	0.6%	0.6%	0.6%
Modelling of z vertex	0.6%	0.8%	0.7%
'MIP' parameter	0.5%	0.5%	0.5%
$\not{E}_{\mathrm{T}}$ smearing parameters	0.3%	0.3%	0.3%
p_T scale	0.2%	0.2%	0.2%
Bias in muon identification efficiency	0.2%	0.2%	0.2%
Bias in tracking efficiency	0.2%	0.2%	0.2%
Total (excluding PDF)	1.4%	1.5%	1.3%
Total	2.0%	1.9%	1.8%

Table 5: Summary of systematic uncertainties on the acceptance.

4.5 Summary of Uncertainties on the Acceptance

A summary of the uncertainties on the acceptance is given in Table (5).

The rest of this section consists of a brief description of each source of uncertainty and it's method of evaluation.

- The uncertainty on the acceptance due to the choice of PDF is evaluated using the method suggested by the CTEQ collaboration and the associated PDF sets [14].

- The uncertainty due to the modelling of the W boson p_T is obtained by comparing the acceptance above with the acceptance obtained using an alternative tune of PYTHIA [16].

- The statistical uncertainty is not due to the size of the Monte Carlo samples used to evaluate the acceptance, but rather due to the uncertainty on the input tracking, trigger and muon identification efficiencies. The accuracy with which these efficiencies are known is determined from the data and the uncertainty is evaluated by varying each of the efficiencies when they are introduced into the simulation. Simultaneously the value of the efficiency in each bin is varied independently with a Gaussian distribution with sigma equal to the size of the uncertainty on that bin. This is done 400 times and the statistical uncertainty is given by the standard deviation of the ϵ values obtained.

- The uncertainty on the isolation is described in section 3, being due to biases in the tag and probe method and $b\bar{b}$ background in the efficiency sample.

- The variation due to the time dependence of the efficiencies is found by evaluating the number of candidates, luminosity and efficiency in blocks of 5pb^{-1}. The average cross section from this method is compared with the central value and the difference used to estimate the uncertainty due to the time dependence of the efficiencies.

- The luminous region as a function of z depends on the configuration of the beam, and so varies with time. The practice that has been adopted here is to tune the width and mean of the z distribution to agree with the average seen in data. The uncertainty in this tuning is propagated through to an uncertainty on the acceptance.

- The acceptance is evaluated using a parameterised model of the DØ detector, which are tuned to data from DØ. These tunes have some uncertainty on them which results in uncertainties on the acceptance. The largest of these uncertainties (0.5%) arises from an uncertainty on the energy deposited by the muon in the calorimeter (the 'MIP' parameter). There are also non-negligible sources of uncertainty from the p_T scale of the tracker (0.2%) and in the hadronic energy scale(0.2%) and hadronic sampling term(0.2%).
- There is an uncertainty on the both the tracking and muon identification efficiencies caused by a small bias in the 'tag and probe' method (see Section 3).

5 Background Estimation

There have been four sources of background identified as contributing to the candidate events, these are listed below:

1. The largest source of contamination is from the 'electroweak' background. This is caused by $Z/\gamma \rightarrow \mu^+\mu^-$ events, where only one of the muons is identified, and $W \rightarrow \tau\nu$ and $Z \rightarrow \tau^+\tau^-$ events which produce one muon from tau decays. The size of this background is estimated with the Monte Carlo simulation used to evaluate the acceptance. The uncertainties arising from these backgrounds will be conservatively treated as fully correlated, background to background.
2. There is a significant contribution to the candidate events from quarks that decay semi-leptonically, producing muons (The 'QCD' Background).
3. A further source of contamination is from mesons, such as pions and kaons, that decay inside the tracking volume ('In flight decays').
4. The last source of background is from cosmic rays.

The latter three backgrounds are all evaluated from data. Throughout the various contaminations are expressed as a fraction relative to the number of $W \rightarrow \mu\nu$ events. The rest of this section gives a more detailed description of each of the backgrounds, the cuts used to reject them and estimates what fraction of the candidate events can be attributed to them.

5.1 Electroweak Background

The three decays of W and Z bosons that can mimic $W \rightarrow \mu\nu$ events are summarised in table 6. This table lists the ratio between the background and signal cross sections (R_σ), the efficiency of the event selection applied to the background sample (ϵ) in the MUW_W_L2M3_TRK10 and MUW_A_L2M3_TRK10 periods and finally the fraction of the candidate events attributed to the particular background (f). The fraction attributable to a given background x is evaluated as follows

$$f_x = \frac{\sigma(x)}{\sigma(p\bar{p} \rightarrow W \rightarrow \mu\nu)} \times \frac{\epsilon(x)}{\epsilon(W \rightarrow \mu\nu)}$$

$$f_x = R_\sigma \times \frac{\epsilon(x)}{\epsilon(\mathrm{W} \to \mu\nu)}$$

All the values of ϵ are evaluated using PMCS.

$Z/\gamma \to \mu^+\mu^-$ events can mimic $W \to \mu\nu$ events if one of the muons lies outside the detector acceptance or if one of the muons is not reconstructed in either the tracker of the muon chambers. A sample of 200k $Z/\gamma \to \mu^+\mu^-(M_{Z/\gamma^*} > 30\ \mathrm{GeV/c^2})$ events is generated using PYTHIA and the efficiency of the $W \to \mu\nu$ even selection evaluated. The ratio of the $Z/\gamma \to \mu^+\mu^-(M_{Z/\gamma^*} > 30\ \mathrm{GeV/c^2})$ to $W \to \mu\nu$ cross sections is taken from a product of the ratio of the $Z \to \mu^+\mu^-$ to $W \to \mu\nu$ cross sections (0.092) and from the ratio of the $Z/\gamma \to \mu^+\mu^-(M_{Z/\gamma^*} > 30\ \mathrm{GeV/c^2})$ to $Z \to \mu^+\mu^-$ cross section (1.30 [17]).

Events where W and Z Bosons decay to τ leptons can pass the event selection if a τ decays to a high p_T muon within the acceptance. The cross section of $W \to \tau\nu$ is identical to that of $W \to \mu\nu$ and that of $Z/\gamma \to \tau^+\tau^-$ identical to $Z/\gamma \to \mu^+\mu^-$. The acceptances for $W \to \tau\nu$ and $Z/\gamma \to \tau^+\tau^-$ are evaluated using samples of 200,000 PYTHIA events for each process.

The uncertainty on these figures arise from the fact that the p_T scale of the isolation cut is not rescaled to either the higher scale of the Z or the lower one associated with the τ. To be conservative a 5% uncertainty is assigned on all values. All other uncertainties such as those describing the modelling of the efficiencies are assumed to largely cancel and hence are neglected.

Background	R_σ	ϵ(all)	ϵ(wide)	f(all)	f(wide)
$W \to \tau\nu$	1.00	0.055	0.047	0.025 ± 0.001	0.025 ± 0.001
$Z/\gamma \to \mu^+\mu^-$	0.118	0.077	0.065	0.043 ± 0.002	0.041 ± 0.002
$Z/\gamma \to \tau^+\tau^-$	0.118	0.0032	0.0027	0.0018 ± 0.0001	0.0017 ± 0.0001

Table 6: Summary of ‘Electroweak’ Backgrounds.

5.2 QCD background

The QCD Background is evaluated from data using the matrix method. The matrix method uses a set of two simultaneous equations to extract the number of signal and background events in the sample.

Firstly the isolation cut, which has a high rejection factor for QCD background events, is removed. Then all other event selection requirements are applied, which results in a total of N events, of which B are background, and S are signal. Then the final event selection is applied, resulting in N_2 events. Two equations result:

$$N = B + S, \tag{14}$$
$$N_2 = fB + \epsilon S, \tag{15}$$

where f and ϵ are the efficiencies for background and signal events to pass the final event selection. Knowing the efficiencies f and ϵ, these equations can be solved to give the number of background events in the final sample:

$$B = \frac{\epsilon N - N_2}{\epsilon - f}. \tag{16}$$

To use the Matrix Method, the signal and background efficiencies have to be measured. This is done using as pure as possible samples of signal and background events. For the signal, efficiencies are obtained in the data on samples of $Z \rightarrow \mu^+\mu^-$ events, which have a high purity as described in section 3.

5.2.1 Fake Rate Estimation

The background efficiency, or fake rate, is obtained using muons with high $\not\!\!E_T$ and low p_T.

Fig. 27 shows the probability for single muons to pass the isolation cut as a function of p_T. This sample of single muons has all the cuts of the event selection applied except those on the p_T $\not\!\!E_T$ M_T and isolation requirements. The different bands are where different $\not\!\!E_T$ and M_T cuts have been applied.

The efficiency for background events is taken from events with $\not\!\!E_T$ > 20 GeV and $M_T >$ 40 GeV/c^2 in the low p_T region, where the probability for a single muon to be isolated is 0.06. In the high p_T region this sample becomes contaminated with $W \rightarrow \mu\nu$ events, which tend to be more efficient.

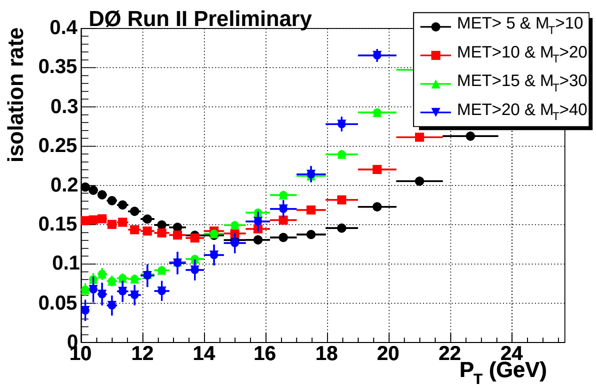

Figure 27: Fraction of isolated events in single muon events as a function of the muon transverse momentum, for different MET requirements.

To extrapolate this efficiency into the high p_T signal region di-muon events are used. The different kinematics of these events means that we cannot use them to get an absolute value, but we do trust that the p_T dependence will be roughly the same.

Fig. 28 shows the probability for the second muon in di-muon events to be isolated. The left hand plot shows this for the case where both muons have opposite signs and the first muon is required to be isolated. The probability drops off with p_T until around 20GeV/c it starts rising as the $Z/\gamma \rightarrow \mu^+\mu^-$ contamination increases, in an analogous manner to that seen for the single muon events in Fig. 27. From this we draw the conclusion that the behaviour of the di-muon and single muon samples are similar.

The right hand plot of Fig. 28 shows the same thing except now that the two muons are required to possess the same sign. Those di-muon pairs with like charges are not contaminated

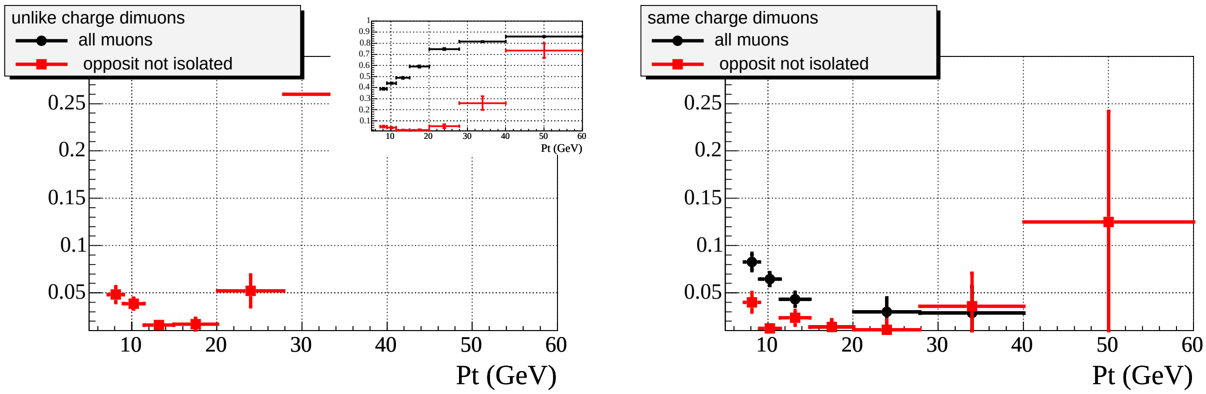

(a) Opposite charge di-muons

(b) Same charge di-muons

Figure 28: Fraction of isolated events in di-muon samples as a function of the muon transverse momentum.

by $Z/\gamma \rightarrow \mu^+\mu^-$ and arise mostly from real $b\bar{b}$ events. These events are produced either by a $B_0\bar{B}_0$ oscillation or by the cascade decay $b \rightarrow cX \rightarrow X'\mu\nu$. Muons produced from cascade decays tend to have lower p_T and tend to be less isolated, than those muons directly from b decays. This can be seen in Fig.28(b), where the red dots are lower than for unlike sign di-muon events.

Observation of Figs. 28(a) and 28(b) shows that the fake rate decreases with p_T. The three different functions (red dots in Fig. 28(a), black and red dots in Fig. 28(b)) show the same decrease with p_T. From this we conclude that the fake rate will also decrease with p_T in single muon events. However it is not clear whether this decrease is linear or exponential and whether the fake rate tends to 0 at high p_T or to some constant value.

The three functions have different values for a given p_T, demonstrating that the fake rate is sensitive to the overall kinematic configuration in a non trivial manner. Therefore it is not possible to extract the fake rate from these di-muon events to the $W \rightarrow \mu\nu$ candidate events. However we do conclude that the fake rate falls as a function of p_T implying that the fake rate at low p_T obtained from Fig. 27 of 0.06 is an upper bound. The final fake rate is quoted to be halfway between this number and 0, with the uncertainty spanning this range, i.e.

$$f = 0.03 \pm 0.03.$$

5.2.2 QCD Background Estimation

To estimate the fake rate all the $W \rightarrow \mu\nu$ event selection cuts, except the isolation requirements, are applied resulting in N events. The isolation cut is then applied leaving N_2 events.

Using the fake rate found above and the isolation efficiency described in section 3 the matrix method can be used to evaluate the QCD background. Table 7 summarises the figures used to obtain the QCD background. Note that the efficiency quoted for the signal is only an average. What is actually used is 80 different values, at intervals in p_T of 1 GeV/c from 20 GeV/c.

Translating the number of QCD background events into a background fraction results in:

Quantity	MUW_A_L2M3_TRK10	MUW_W_L2M3_TRK10
N	41579	46777
N_2	29159	33126
fB	228	238
ϵ	0.843 ± 0.008	0.847 ± 0.008
f	0.03 ± 0.03	0.03 ± 0.03
f_{QCD}	0.008 ± 0.008	0.007 ± 0.007

Table 7: Summary of Figures used to Evaluate the QCD Background.

$$f_{QCD} = (0.7 \pm 0.7)\% \text{ in the MUW\_W\_L2M3\_TRK10 sample}$$

$$f_{QCD} = (0.8 \pm 0.8)\% \text{ in the MUW\_A\_L2M3\_TRK10 sample.}$$

The uncertainty is dominated by that on the fake rate.

The kinematic spectra of the QCD background, as calculated by the matrix method, is shown in Figs. 35, 36 and 37. It shows a smooth exponential behaviour, providing confidence that this method produces reasonable results.

5.3 Muons from In-Flight Decays and Cosmic Rays Background

Mesons, such as kaons and pions, have high branching fractions into a $\mu\nu$ pair; for kaons 63.4% and for pions 99.99%. They also have decay lengths similar to the radius of the central tracker (52 cm); for kaons $c\tau = 3.7$ m and for pions $c\tau = 7.8$ m. This can produce an isolated muon in the muon chambers in association with a track in the central detector, faking a W $\rightarrow \mu\nu$ event. Collectively these events are known as 'in-flight decays' (IFDs).

Trying to fit a single track from the combination of two tracks tends to produce a larger χ^2 in the track fit and poorer dca and p_T resolution. Combining this poor p_T resolution with the fact that the muon produced in the decay tends to have lower p_T results in a discrepancy between the p_T as measured by the muon system and that as measured by the central tracker.

Cosmic rays can pass the W $\rightarrow \mu\nu$ event selection if they are reconstructed in both the muon system and the tracker. As they are not produced in the interaction point, they tend to have large value. It is the dca distribution that is used to discriminate the signal events from the backgrounds. The procedure adopted is to create template dca distributions for signal and backgrounds. The dca distribution is then fitted with a sum of these templates to estimate the fraction of candidates that are due to 'in flight decay' and cosmic backgrounds.

5.3.1 Obtention of dca Distribution in Signal Events

The template dca distribution in signal events is obtained from Z $\rightarrow \mu^+\mu^-$ events, assuming that the dca distribution in W $\rightarrow \mu\nu$ events is the same. A clean sample of Z $\rightarrow \mu^+\mu^-$ events is obtained by requiring that:

1. Both muons have p_T greater than 20 GeV/c.

2. Both muons are isolated with opposite charges.

3. The invariant mass of the di-muon system is greater than 75 GeV/c^2.

4. The acolinearity, A, defined as $A = \pi - |\phi_1 - \phi_2| + |\theta_1 + \theta_2 - \pi|$, is greater than 0.025.

A sample dominated by cosmic muons is obtained using this selection, but reversing the acolinearity cut. A sample dominated by $b\bar{b}$ background is obtained using this selection but reversing the isolation criteria or the opposite-charge requirement.

Figure 29(a) shows the log10(|dca|) distribution for the various requirements. The cosmic background (events failing acolinearity) and the Z $\rightarrow \mu^+\mu^-$ events have very distinct signatures, whereas it can be seen that the *dca* variable has low discriminating power against $b\bar{b}$ events.

The dca distribution in the Z $\rightarrow \mu^+\mu^-$ events is used as a template for the signal events. As an indication that using Z $\rightarrow \mu^+\mu^-$ events to obtain the dca distribution in W $\rightarrow \mu\nu$ events is valid, the W $\rightarrow \mu\nu$ and Z $\rightarrow \mu^+\mu^-$ dca distributions are overlaid in Fig. 29(b), which can be seen to agree well in the low dca region which is expected to be dominated by signal.

Similarly the template for cosmic events is taken from the cosmic distribution which can be seen in Fig. 29(a).

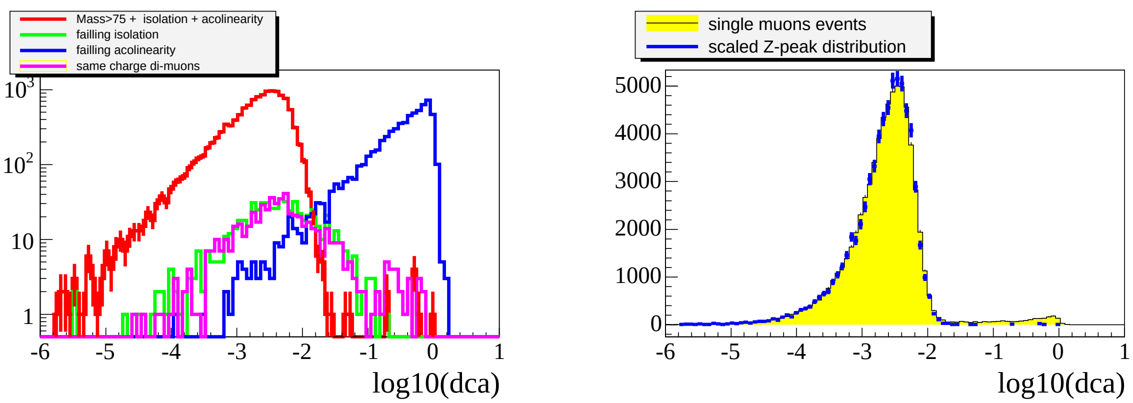

(a) log10(|dca|) in di-muon events

(b) log10(|dca|) in the W $\rightarrow \mu\nu$ candidate sample, compared with the shape from Z events

Figure 29: log10($|dca|$) in di-muon and single muon events

5.3.2 Obtention of dca distribution in In Flight Decay Events

To study the dca distribution of in flight decay and cosmic ray events we first need to select a sample enhanced in these backgrounds. In flight decay events are identified using the fact that the p_T as measured by the local muon system tends to be low. The first step is to identify what the local p_T looks like for the signal.

This is done by looking at the local p_T in Z $\rightarrow \mu^+\mu^-$ events as shown in Fig. 30. This sample is selected requiring two isolated, high momentum ($p_T > 15$ GeV/c) muons with hits in the silicon detector and requiring $|dca| < 110$ μm for each track. The resulting mass distribution from this selection is show in Fig. 30. The local p_T is plotted for both muons in events that possess a mass between 60 and 120 GeV/c^2.

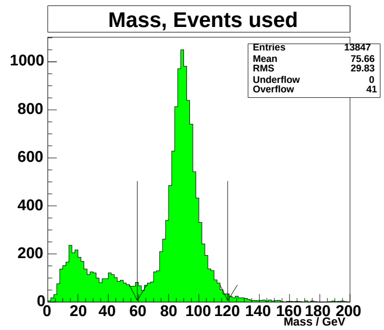

(a)

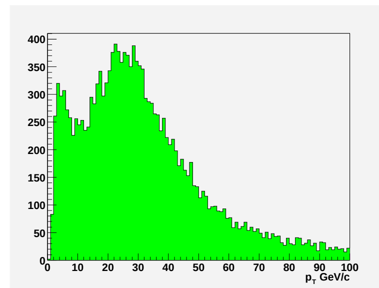

(b)

Figure 30: (a) Histogram showing the di-muon invariant mass distribution resulting from the $Z \rightarrow \mu^+\mu^-$ event selection. The distribution of local momentum for muons in events with a mass between 60 and 120 GeV/c^{2}is shown in (b).

The local p_T as measured in the final W sample is shown in Fig. 31, for the MUW_W_L2M3_TRK10 period. Fig. 31 also shows the local p_T distribution after removing either the χ^2/d.o.f. or dca cuts, or both of these cuts.

Fig. 31 indicates that the events with local $p_T < 10$ GeV/c are dominated by background, and that events with local $p_T > 25$ GeV/c are dominated by signal. This demonstrates that samples enhanced in 'in flight' decay background can be obtained by removing the χ^2 cut or by cutting on local p_T.

Samples enriched in in flight decays are obtained in three ways:

1. By applying all the $W \rightarrow \mu\nu$ event selection, with the exception of that on the χ^2 of the central track.

2. By applying all the $W \rightarrow \mu\nu$ event selection and additionally requiring that local p_T is less than 10 GeV/c.

3. By applying all the $W \rightarrow \mu\nu$ event selection, with the exception of that on the χ^2 of the central track and additionally requiring that local p_T is less than 10 GeV/c.

Figures 32(a), (c) and (e) shows the $log(|\text{dca}|)$ distribution obtained for these three samples.

To obtain the IFD templates first the $W \rightarrow \mu\nu$ and cosmic contributions must be subtracted. These templates are scaled to fit the distributions seen in Fig. 32. For $W \rightarrow \mu\nu$ the fit is performed in the range $[-4, -2.5]$, whilst for the cosmic events it is performed in the range $[-0.1, 0.2]$. The three in flight decay templates are extracted by subtracting the signal and cosmic contributions from the full distributions. The IFD background is then evaluated by fitting this template, along with those for cosmic and signal events, to the candidate event dca sample. This is shown in Figs. 32(b), (d) and (f). This is then used to extract the fraction of events attributed to in flight decay and cosmic ray backgrounds.

The background fractions using the templates obtained from the three samples are listed in Table 8. The process is carried out with and without QCD background subtraction. In all cases the cosmic background, for $|\text{dca}| < 110\,\mu$m, is found to be negligible.

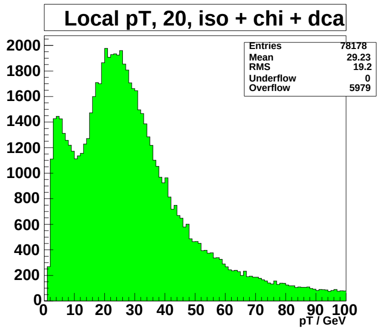

(a)

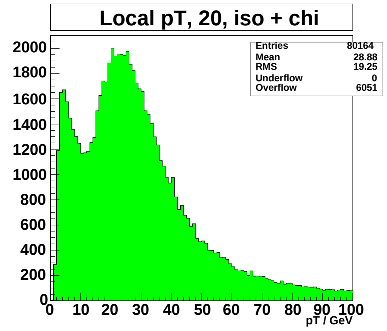

(b)

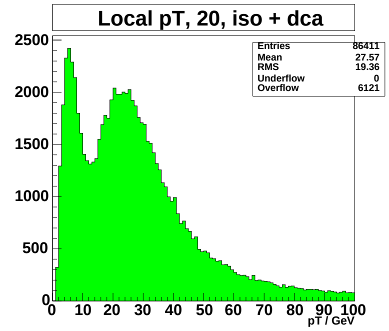

(c)

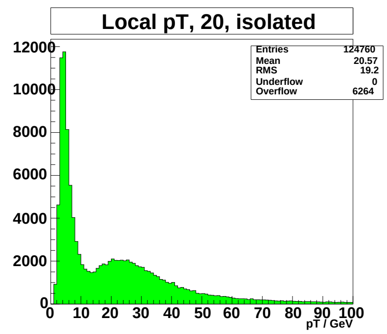

(d)

Figure 31: (a) Histogram of the local p_T passing all the $\mathrm{W} \rightarrow \mu\nu$ selection cuts in the MUW_W_L2M3_TRK10 period. The local p_T distributions resulting from removing (b) the dca cut, (c) the χ^2/d.o.f. cut and (d) both the dca and χ^2/d.o.f. cuts.

The 'average' is based upon the template fitted using the sample with the same χ^2 as the event selection applied. This is justified based upon the examination of Fig. 32(e), which shows that the χ^2 cut does slightly alter the *dca* shape for the IFD background. Therefore the dca distribution as taken from this plot is likely to be closest to that in the candidate events, even if it is limited by statistics. To cover the range of all different estimates, a systematic error of 0.12% is assigned and we quote $0.22 \pm 0.12\%$ as being the IFD contamination.

5.3.3 System 8 Evaluation of In-Flight Decay Background

As a cross check the fraction of the candidate events attributable to IFD is also evaluated using *system 8*, which is essentially the matrix method applied in two dimensions [9]. The advantage of *system 8* over the standard matrix method is that it avoids the difficulty of having to select samples of pure background which realistically model the background present in the $\mathrm{W} \rightarrow \mu\nu$ sample.

To use system 8, the sample is divided into two datasets,which contain different proportions of signal and background events. The two samples used are events with local p_T< 10 GeV/c

Sample	f_{IFD}	f_{cos}
1	0.0010	< 0.0004
2	0.0013	< 0.0004
3	0.0022	< 0.0004
1 (+ QCD)	0.0012	< 0.0004
2 (+ QCD)	0.0016	< 0.0004
3 (+ QCD)	0.0026	< 0.0004
'Average'	0.0022 ± 0.0012	negligible

Table 8: Summary of Background Estimates For Cosmic rays and In Flight Decays.

and one with local $p_T > 25$ GeV/c. The distribution of local p_T with and without the χ^2/d.o.f. and dca cuts applied is shown in Fig. 31. Then, the standard W $\rightarrow \mu\nu$ selections are applied, apart from the two selections which have the highest rejection power against the background to be measured. For the IFD background the dca and χ^2/d.o.f. cuts are used. These two cuts are then applied in turn, resulting in these equations:

$$N = B + S \tag{17}$$

$$N_2 = \alpha B + \gamma S \tag{18}$$

$$N_3 = \beta B + \delta S \tag{19}$$

$$N_4 = \alpha\beta B + \gamma\delta S \tag{20}$$

where α, β, γ and δ are the efficiencies for background and signal events to pass the event selections. Applying this procedure to both datasets results in a total of 8 equations, which can be solved for the number of signal events, and each of the efficiencies. System 8 is described in more detail in [9]. Once the signal and background efficiencies have been extracted using system 8, they can be used in a matrix method, in which both selections are applied simultaneously, to obtain the number and distribution of background events in the final sample.

One potential issue is that relaxing the *dca* cut will allow some additional QCD background into the sample. So, to test the stability of the results, the calculation is performed using various isolation cuts to reject more or less QCD background. Also, the central track p_T and $\not{E}_T$ cuts are decreased from 20 GeV/c to 15 GeV/c to produce a sample with more background.

The results are summarised in Table 9, and are stable under these variations. This stability reflects the fact that the isolation cut has a high rejection for the QCD events, and there is little contamination remaining in the sample. The signal efficiencies resulting from the system 8 method are in good agreement with efficiencies measured on a sample of Z $\rightarrow \mu^+\mu^-$ events. Repeating the system 8 method with the signal efficiencies fixed to the values measured on the Z $\rightarrow \mu^+\mu^-$ sample produces consistent results.

The signal and background efficiencies are then used in a matrix method (with the cuts on dca and χ^2/d.o.f. applied simultaneously) to obtain the fraction of in-flight events in the final sample. Varying the signal and background efficiencies within the system 8 uncertainties produces a spread in results for the background in the final sample. A systematic uncertainty is assigned to cover the full range of this variation. The in-flight decay background calculated in this way is found to be $0.16 \pm 0.06\%$, which is in good agreement with the fraction calculated above.

The local p_T distributions resulting from the in-flight decay background calculation are shown in Fig. 33, where the distribution of signal and background can be seen.

p_T and $\not{E}_T$ cuts	Isolation cuts	Data	χ^2/d.o.f. efficiency	dca efficiency
(20,20)	(2.5,3.5)	Signal	0.974 $\pm$ 0.002	0.989 $\pm$ 0.002
		Background	0.028 $\pm$ 0.006	0.128 $\pm$ 0.006
(20,20)	(1.5,2.5)	Signal	0.973 $\pm$ 0.002	0.990 $\pm$ 0.002
		Background	0.026 $\pm$ 0.007	0.123 $\pm$ 0.007
(20,20)	(2.5,1.7)	Signal	0.976 $\pm$ 0.004	0.988 $\pm$ 0.004
		Background	0.043 $\pm$ 0.009	0.134 $\pm$ 0.008
(15,20)	(2.5,3.5)	Signal	0.974 $\pm$ 0.002	0.989 $\pm$ 0.002
		Background	0.029 $\pm$ 0.005	0.130 $\pm$ 0.005
(15,20)	(1.5,2.5)	Signal	0.975 $\pm$ 0.002	0.990 $\pm$ 0.002
		Background	0.026 $\pm$ 0.007	0.125 $\pm$ 0.006
(15,20)	(2.5,1.7)	Signal	0.978 $\pm$ 0.004	0.984 $\pm$ 0.004
		Background	0.039 $\pm$ 0.009	0.138 $\pm$ 0.007
(20,15)	(2.5,3.5)	Signal	0.974 $\pm$ 0.002	0.989 $\pm$ 0.002
		Background	0.029 $\pm$ 0.005	0.135 $\pm$ 0.005
(20,15)	(1.5,2.5)	Signal	0.975 $\pm$ 0.002	0.990 $\pm$ 0.002
		Background	0.026 $\pm$ 0.006	0.129 $\pm$ 0.006
(20,15)	(2.5,1.7)	Signal	0.978 $\pm$ 0.004	0.985 $\pm$ 0.004
		Background	0.038 $\pm$ 0.008	0.137 $\pm$ 0.008

Table 9: A summary of the system 8 results for in-flight decays. The isolation cuts are indicated by (x, y), where x is the cut placed on calorimeter isolation, y the cut on track isolation.

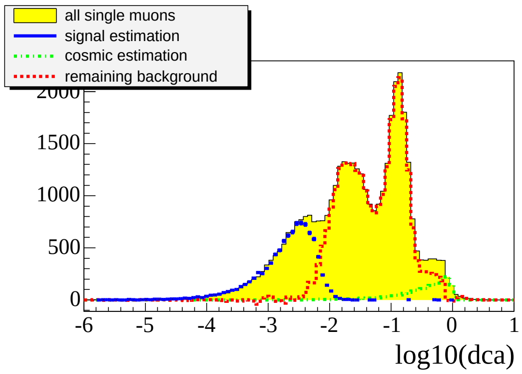

(a) no tracking χ^2 cut, local $P_T < 10$ GeV/c

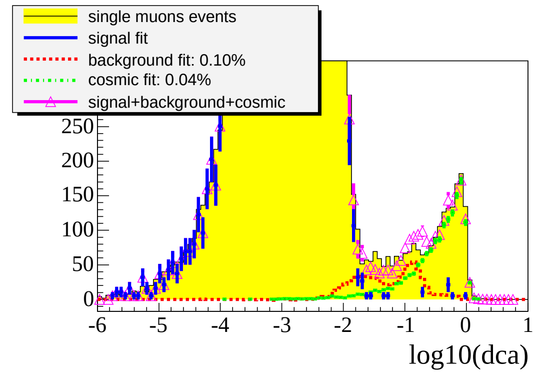

(b) Determination of IFD and cosmic background using IFD shape from (a)

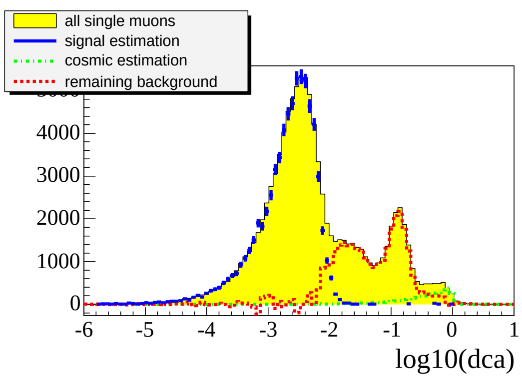

(c) no tracking χ^2 cut

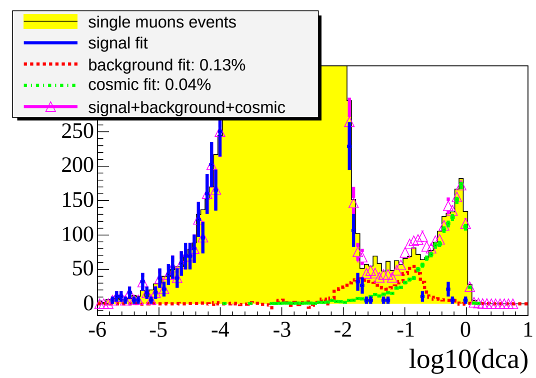

(d) Determination of IFD and cosmic background using IFD shape from (c)

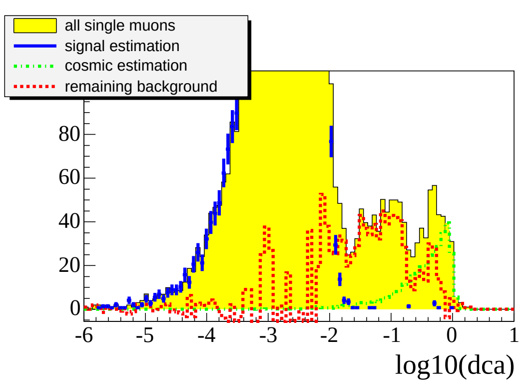

(e) $\chi^2 < 3.3$, $p_T^{\text{local}} < 10$ GeV/c

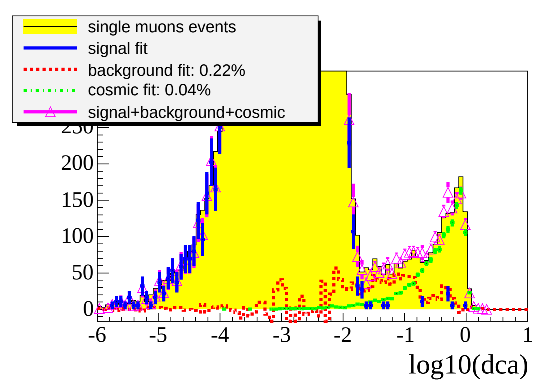

(f) Determination of IFD and cosmic background using IFD shape from (e)

Figure 32: log10(|dca|) distributions. In (a), (c) and (e), different cuts are used to enhanced the IFD fraction. For each case, the IFD shape (in red) is subtracted after fitting the expected signal and cosmic distribution using the templates obtained from the di-muon sample Fig. 29(a). Then a fit to the dca distribution in the W $\rightarrow \mu\nu$ candidate sample is performed to obtain the fraction of IFD and cosmic muons ((b), (d) and (f)).

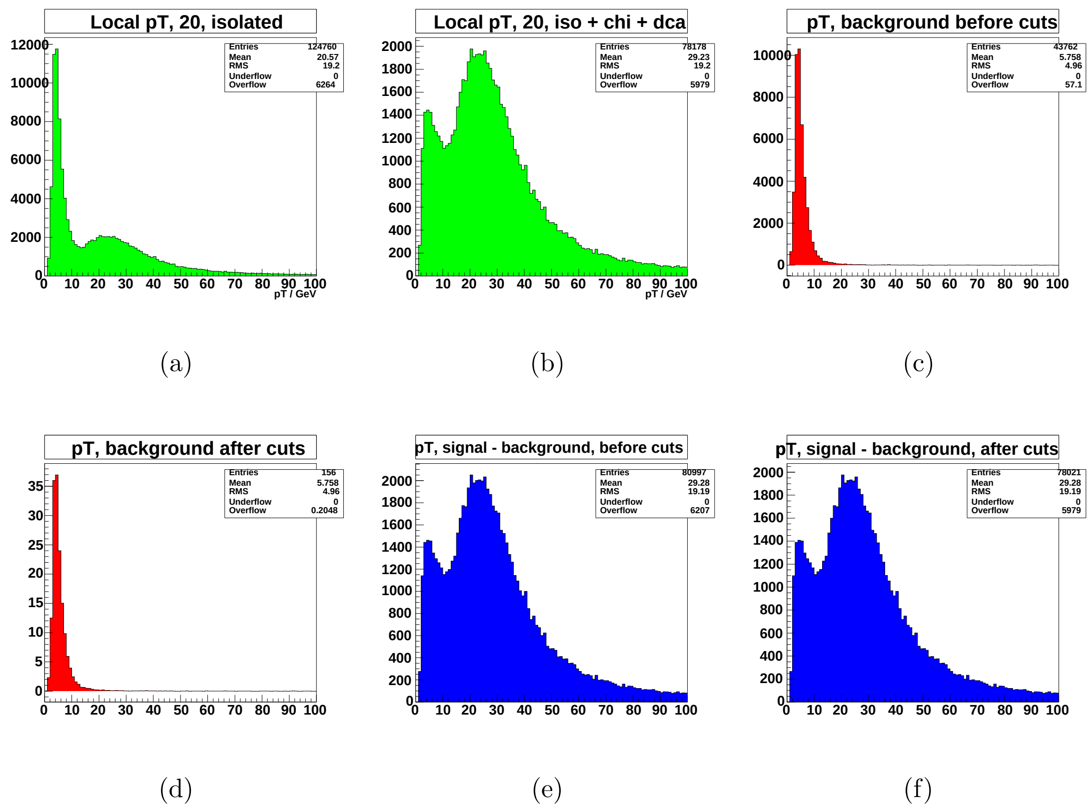

Figure 33: Distributions of local p_T (a) before and (b) after applying the χ^2/d.o.f. and dca cuts. The calculated background distribution (c) before and (d) after applying the cuts. The background subtracted distribution (e) before and (f) after applying the cuts.

6 Results

6.1 Cross-Section Computation

The inclusive W $\rightarrow \mu\nu$ production cross section is calculated using this formula:

$$\sigma(p\bar{p} \rightarrow WX) \times \mathrm{Br}(\mathrm{W} \rightarrow \mu\nu) = \frac{\mathrm{N_{data}}}{\epsilon \times \mathcal{L}} \times \frac{(1 - f_{QCD} - f_{IFD})}{(1 + f_{EW})} \tag{21}$$

where N_{data} is the number of selected events, f_{EW} is the fraction of electroweak background computed with respect to the number of W events, f_{QCD} and f_{IFD} are the fractions of QCD and IFD backgrounds computed with respect to the number of candidate events, ϵ is the overall efficiency and acceptance and $\mathcal{L}$ is the integrated luminosity. The numerical values for this formula are given in Table 10.

Sample	'Wide' Region	'All' Region
Number of candidates	33126	29159
Acceptance	22.37 %	25.59%
Isolation efficiency	84 7%	84.3 %
Electroweak background	6.7%	7.0%
IFD and cosmic background	0.25 %	0.25%
QCD background	0.7 %	0.8 %
Luminosity	53.7 pb^{-1}	41.9 pb^{-1}
Cross-section	3020 pb	2984 pb

Table 10: Result summary

In Table 11 we summarize the different fractional contributions to the uncertainty of the cross-section measurement. Some of these uncertainties arise from cross-checks performed in Section 7. This allows to write the following results.

For MUW_W_L2M3_TRK10 sample we obtain:

$$\sigma(p\bar{p} \rightarrow WX) \times \mathrm{Br}(\mathrm{W} \rightarrow \mu\nu) = 3020 \;\pm 16(\mathrm{stat}) \;\pm 114(\mathrm{syst}) \;\pm 196(\mathrm{lumi})\ \mathrm{pb}.$$

For MUW_A_L2M3_TRK10 sample we obtain:

$$\sigma(p\bar{p} \rightarrow WX) \times \mathrm{Br}(\mathrm{W} \rightarrow \mu\nu) = 2984 \;\pm 17(\mathrm{stat}) \;\pm 81(\mathrm{syst}) \;\pm 194(\mathrm{lumi})\ \mathrm{pb}.$$

Table 11 contains the covariance terms needed to combine these results. The combined result is a weighted average of the two measurements. The weight of the MUW_W_L2M3_TRK10 is 15% (and 85% for MUW_A_L2M3_TRK10)[6].

$$\sigma(p\bar{p} \rightarrow WX) \times \mathrm{Br}(\mathrm{W} \rightarrow \mu\nu) = 2989 \pm 15(\mathrm{stat}) \pm 80(\mathrm{sys}) \pm 194(\mathrm{lumi})\mathrm{pb}.$$

For testing the two measurements compatibility, we use the covariance matrix and perform a χ^2 test. We obtain: $\chi^2_{meas} = 0.15$. Its probability is $P(\chi^2 > \chi^2_{meas}) = 70\%$.

Figure 34 and Tables 12,13 summarized the measurements at Tevatron.

[6] If the covariance matrix is V_{ij} $(i, j = 1, 2)$ the weight given to measurement i is $\frac{V_{jj} - V_{ij}}{V_{jj} + V_{ii} - 2V_{ij}}$. One obtains the usual $\frac{V_{ii}^{-1}}{V_{ii}^{-1} + V_{jj}^{-1}}$ when V_{ij} is 0.

Source of Uncertainty	'Wide' Region Sample	'All' Region Sample	$\sqrt{\text{covariance}}$
Statistical	0.55 %	0.58 %	0
Isolation efficiency	0.9 %	0.9 %	0
QCD background	0.7 %	0.8 %	0.75×10^{-2}
Electroweak background	0.36 %	0.37 %	0.37×10^{-2}
PDF uncertainty	1.4 %	1.2 %	1.3×10^{-2}
PMCS acceptance (Z stat.)	0.9 %	0.9 %	0.9×10^{-2}
Bias in tracking efficiency	0.2 %	0.2 %	0.2×10^{-2}
Bias in muon Id efficiency	0.3 %	0.3 %	0.3×10^{-2}
p_T scale	0.2 %	0.2 %	0.2×10^{-2}
MIP tune	0.5 %	0.5 %	0.5×10^{-2}
$\not\!\!E_\mathrm{T}$ smearing	0.3 %	0.3 %	0.3×10^{-2}
Modelling of the z vertex	0.8 %	0.6 %	0.69×10^{-2}
Modelling of W p_T	0.2 %	0.2 %	0.2×10^{-2}
Time variation of efficiencies	0.6 %	0.6 %	0.6×10^{-2}
Modelling of Veto criteria	1.5 %	1.5 %	1.5×10^{-2}
Variation with kinematical cuts	2.5 %	0	0
Total relative uncertainty	3.8 %	2.8 %	2.7×10^{-2}

Table 11: Relative uncertainties contributing to the total uncertainty. For each term we assume either 0% or 100% correlation, so that the covariance terms are either 0 or the geometrical average of the two uncertainties. The covariance matrix is given by the square of the last row numbers.

Process	Luminosity	CDF Result
$W \to e\nu$	72 pb^{-1}	2780 ± 14 (stat) ± 60 (syst) ± 166 (lumi) pb [19]
$W \to \mu\nu$	72 pb^{-1}	2768 ± 16 (stat) ± 64 (syst) ± 166 (lumi) pb [19]
$W \to \tau\nu$	72 pb^{-1}	2620 ± 70 (stat) ± 210 (syst) ± 160 (lumi) pb

Table 12: Summary of the W cross-section measurements by CDF Run II.

6.2 Comparison between Data and Monte Carlo

The data and expected background distributions are shown in Figs. 35, 36, 37, 38, 39, 40, 41 and 42. In these plots the QCD background is extracted from the data using the matrix method described in Section 5.2. The electroweak background is obtained from the PMCS simulation. Backgrounds are normalized relatively to the found W cross-section.

Process	Luminosity	DØ Results
$W \to e\nu$	177.3 pb^{-1}	2865 ± 8.3 (stat) ± 62.8 (syst) ± 40.4 (pdf) ± 186.2 (lumi) pb
$W \to \mu\nu$	96 pb^{-1}	2989 ± 15 (stat) ± 81 (syst) ± 194 (lumi) pb

Table 13: Summary of the W cross-section measurements by DØ Run II.

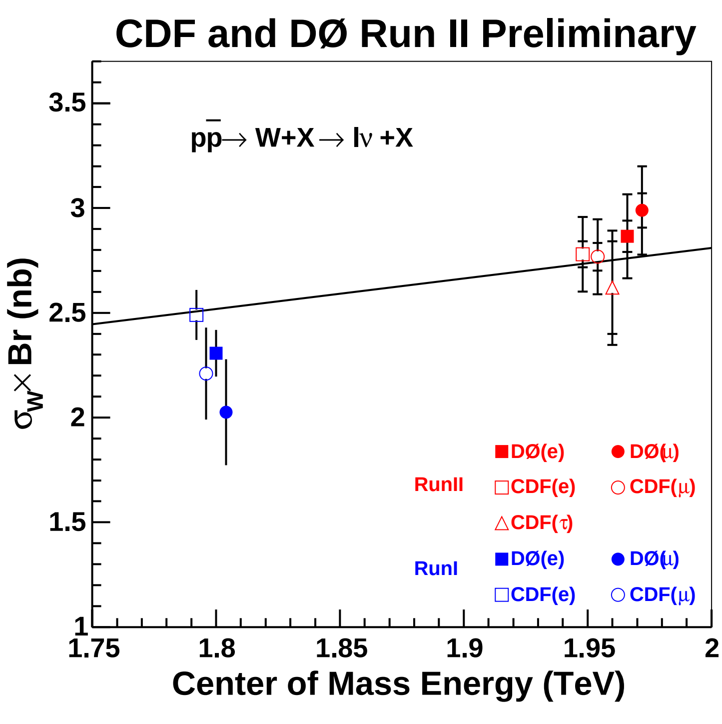

Figure 34: Summary of the W and Z cross-section measurements at Tevatron.

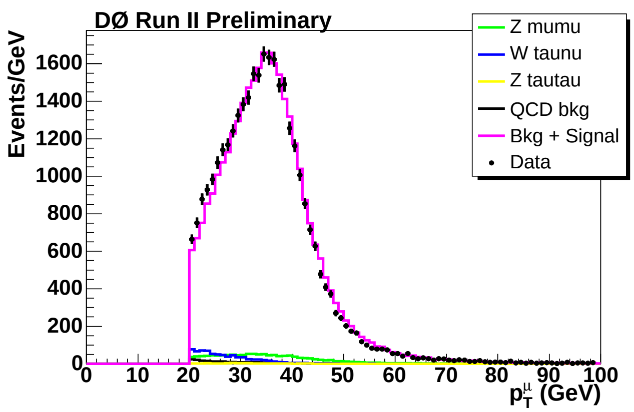

(a) MUW_W_L2M3_TRK10 sample, linear scale.

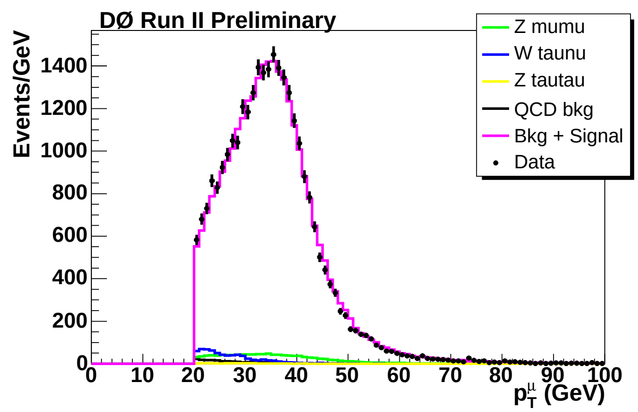

(b) MUW_A_L2M3_TRK10 sample, linear scale.

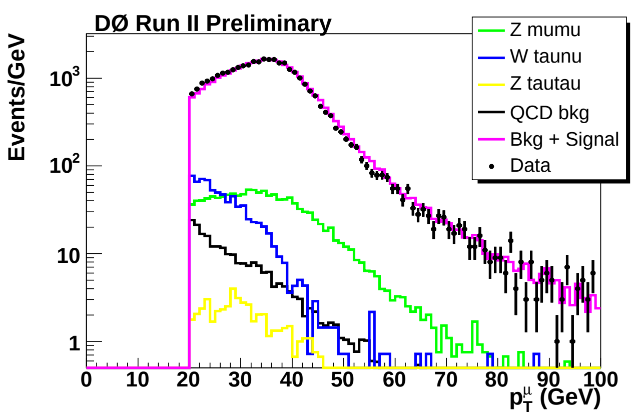

(c) MUW_W_L2M3_TRK10 sample, logarithmic scale.

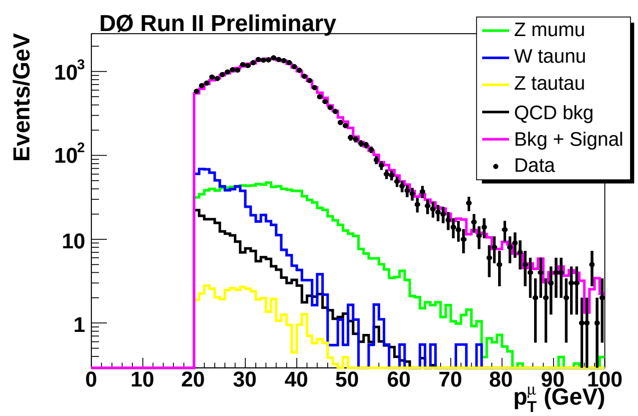

(d) MUW_A_L2M3_TRK10 sample, logarithmic scale.

Figure 35: Distribution of the muon p_T.

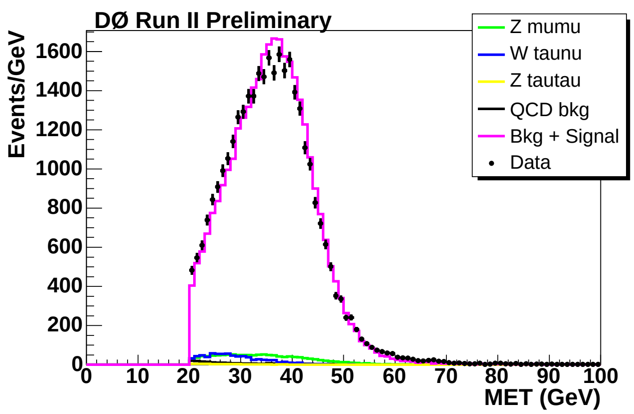

(a) MUW_W_L2M3_TRK10 sample, linear scale.

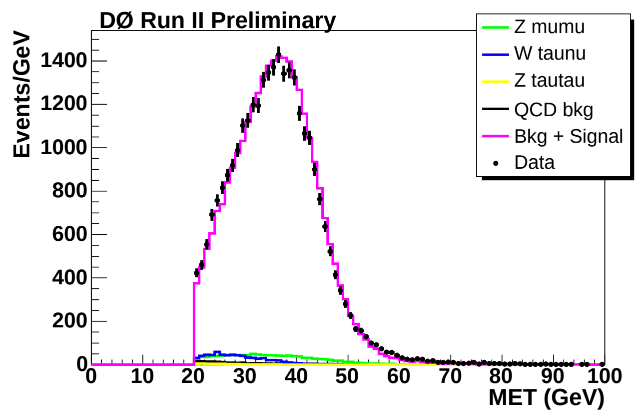

(b) MUW_A_L2M3_TRK10 sample, linear scale.

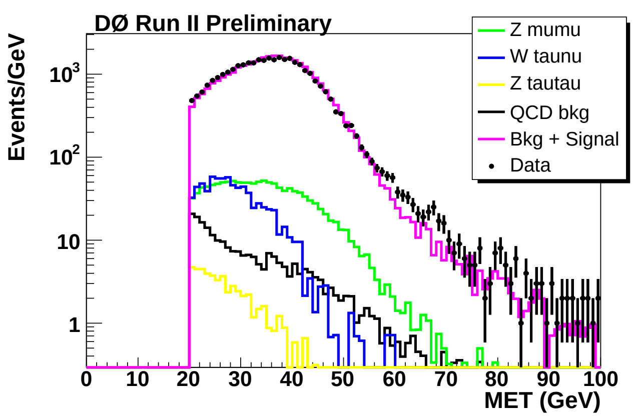

(c) MUW_W_L2M3_TRK10 sample, logarithmic scale.

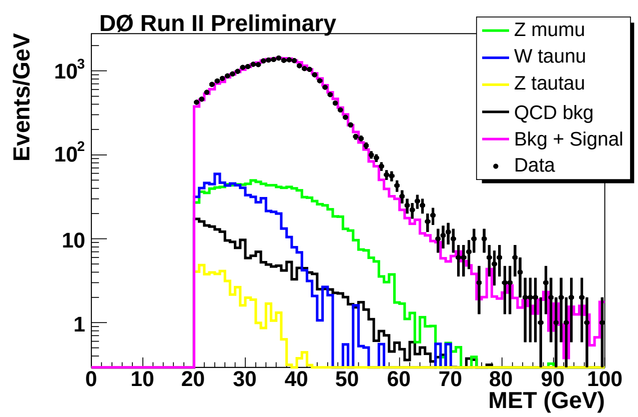

(d) MUW_A_L2M3_TRK10 sample, logarithmic scale.

Figure 36: Distribution of the missing transverse energy.

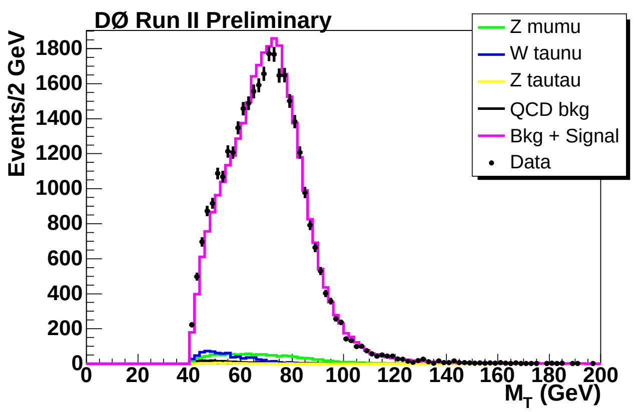

(a) MUW_W_L2M3_TRK10 sample, linear scale.

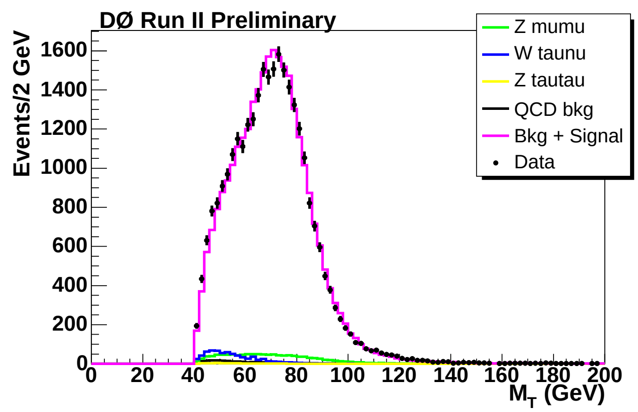

(b) MUW_A_L2M3_TRK10 sample, linear scale.

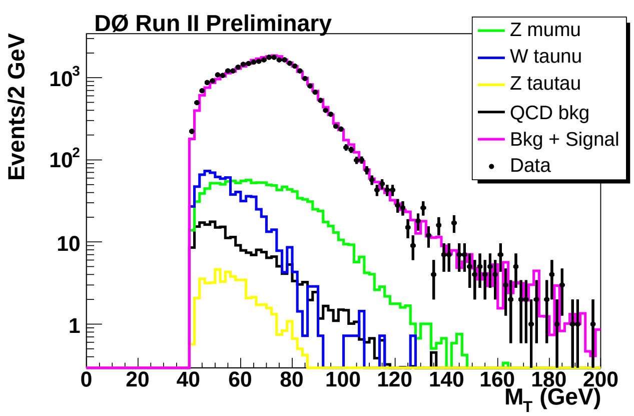

(c) MUW_W_L2M3_TRK10 sample, logarithmic scale.

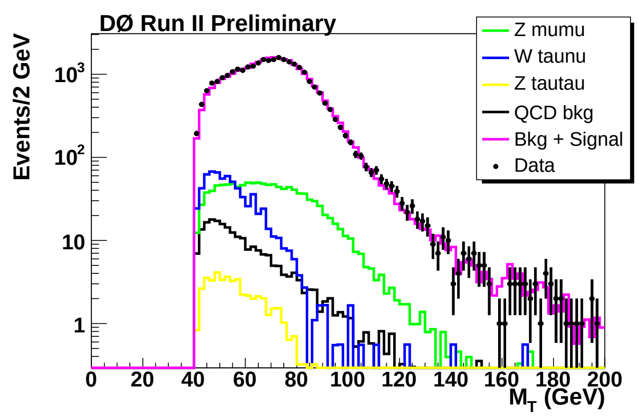

(d) MUW_A_L2M3_TRK10 sample, logarithmic scale.

Figure 37: Distribution of the transverse mass.

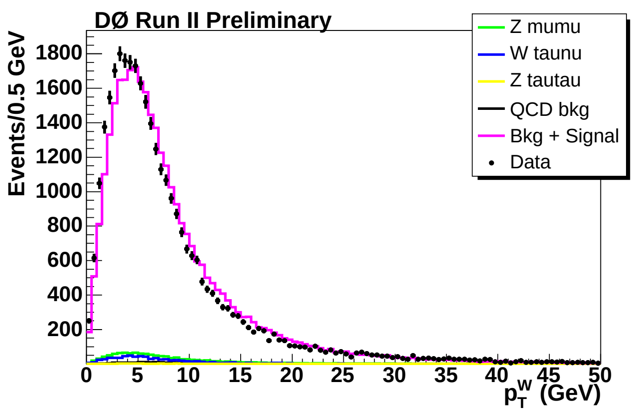

(a) MUW_W_L2M3_TRK10 sample, linear scale.

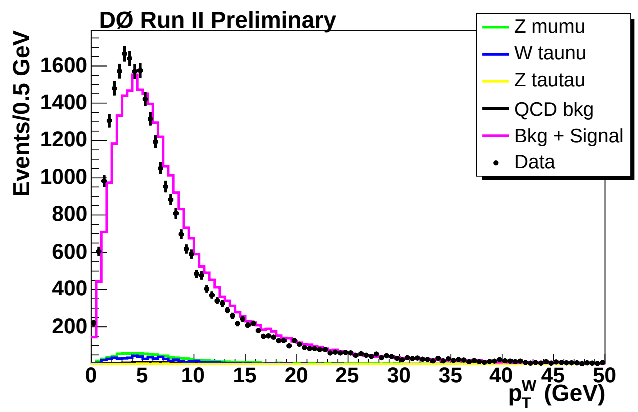

(b) MUW_A_L2M3_TRK10 sample, linear scale.

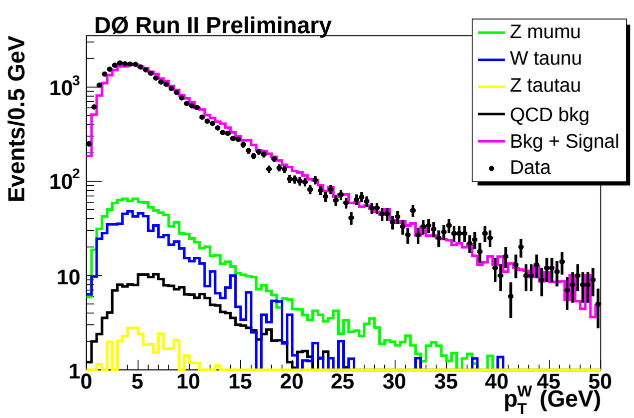

(c) MUW_W_L2M3_TRK10 sample, logarithmic scale.

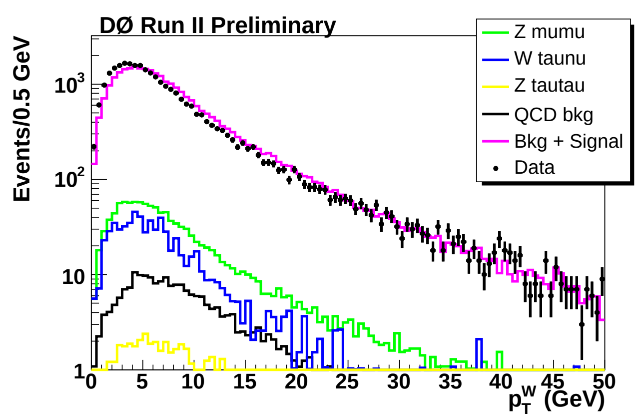

(d) MUW_A_L2M3_TRK10 sample, logarithmic scale.

Figure 38: Distribution of the boson p_T.

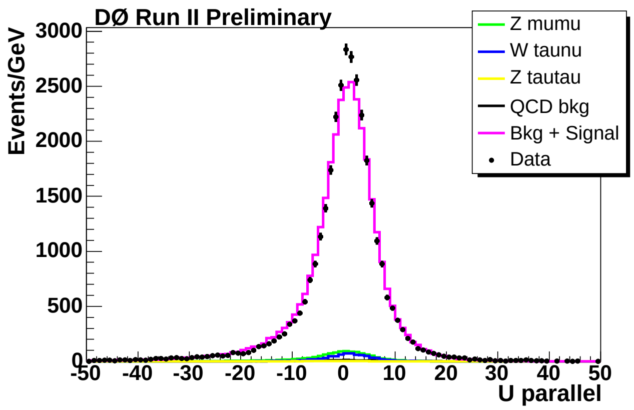

(a) MUW_W_L2M3_TRK10 sample, linear scale.

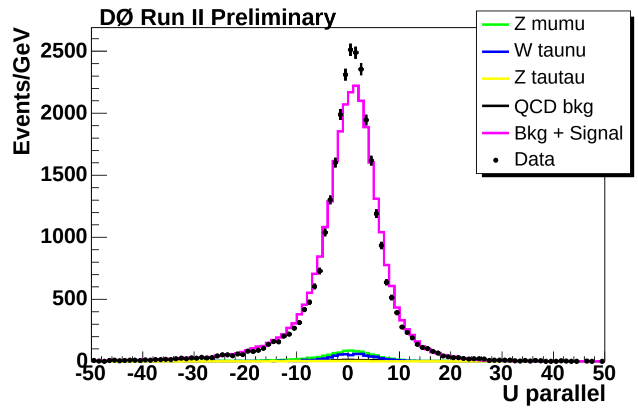

(b) MUW_A_L2M3_TRK10 sample, linear scale.

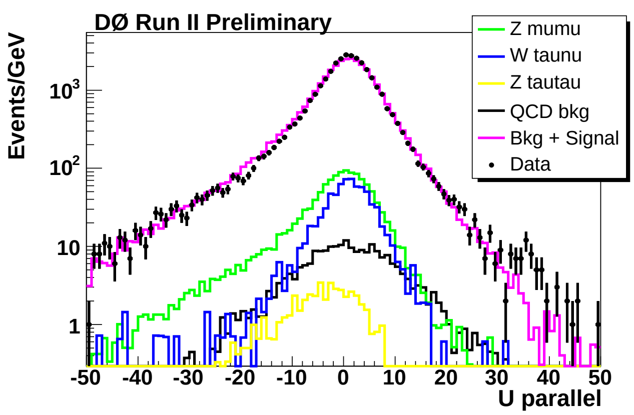

(c) MUW_W_L2M3_TRK10 sample, logarithmic scale.

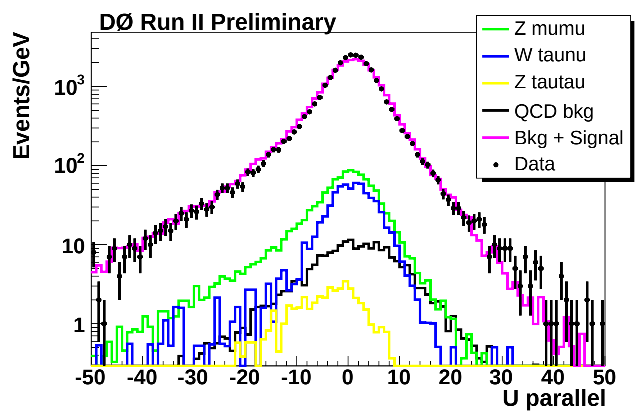

(d) MUW_A_L2M3_TRK10 sample, logarithmic scale.

Figure 39: Distribution of the W recoil projected onto the muon direction ($u_{\parallel}$).

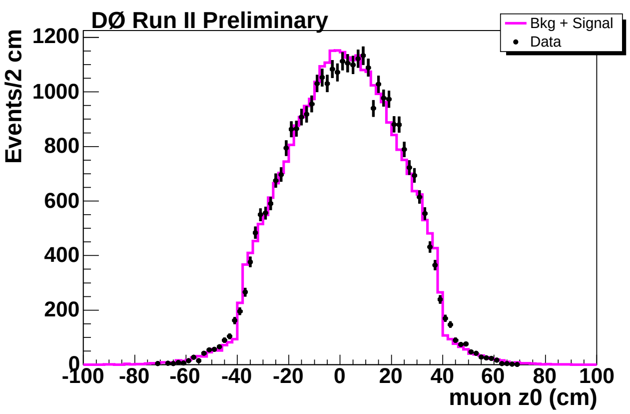

(a) MUW_W_L2M3_TRK10 sample, linear scale.

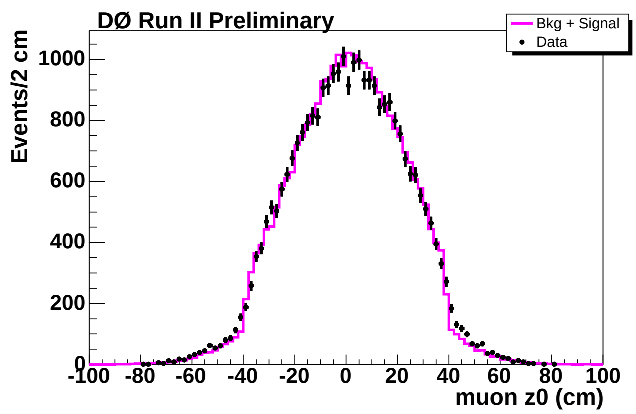

(b) MUW_A_L2M3_TRK10 sample, linear scale.

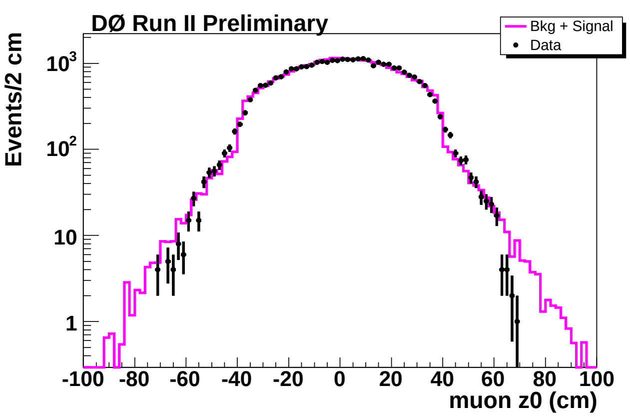

(c) MUW_W_L2M3_TRK10 sample, logarithmic scale.

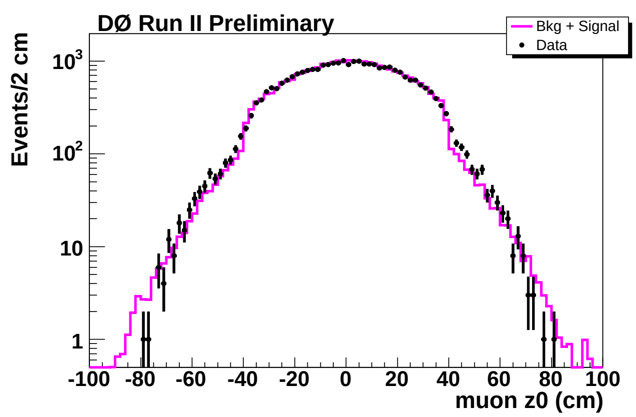

(d) MUW_A_L2M3_TRK10 sample, logarithmic scale.

Figure 40: Distribution of the vertex z position.

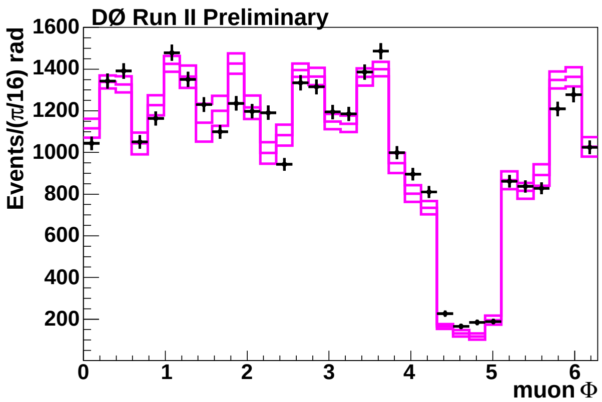

(a) MUW_W_L2M3_TRK10 sample, linear scale.

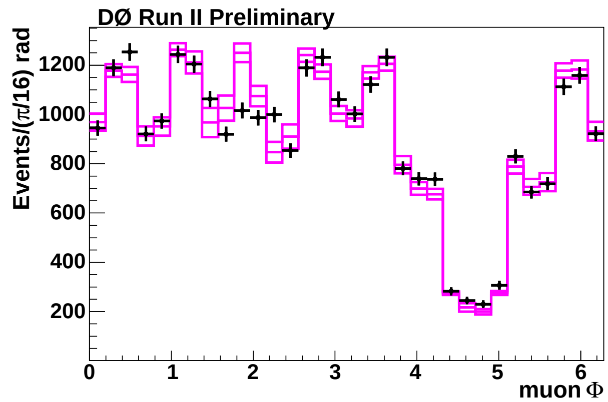

(b) MUW_A_L2M3_TRK10 sample, linear scale.

Figure 41: Distribution of muon azimuthal angle. The different solid lines correspond to the $\pm 1\sigma$ uncertainty due to limited Z statistics in the determination of efficiencies.

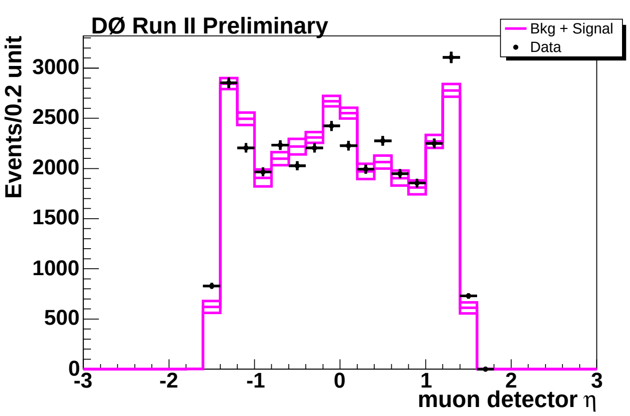

(a) MUW_W_L2M3_TRK10 sample, linear scale.

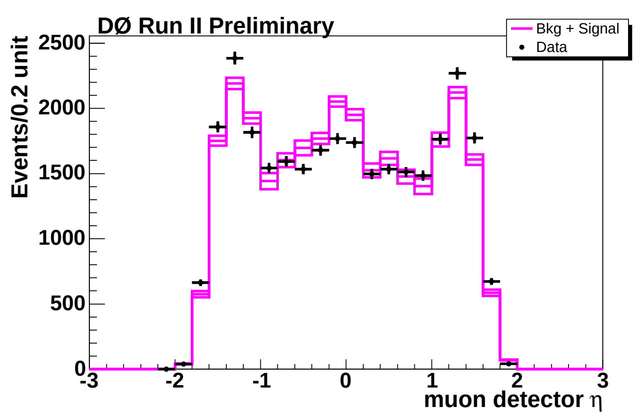

(b) MUW_A_L2M3_TRK10 sample, linear scale.

Figure 42: Distribution of muon detector rapidity. The different solid lines correspond to the $\pm 1\sigma$ uncertainty due to limited Z statistics in the determination of efficiencies.

7 Cross Checks

7.1 Cross-section in different rapidity ranges

The section is computed in different rapidity range as shown in Fig. 43(a). The bin to bin variation on this plot is larger than the expected fluctuations. We understand this variation as being due to the isolation efficiency dependence as a function of the rapidity, shown in Fig. 21(b). This dependence is fitted using the following function:

$$\epsilon(\eta) = A \qquad\qquad\qquad \text{for } 1 > |\eta| \tag{22}$$
$$\epsilon(\eta) = A \quad +A.B(|\eta| - 1) \quad \text{for } 1 < |\eta|. \tag{23}$$

The slope is found to be $B \simeq 5\%$. The cross section as a function of the rapidity is corrected for the variation of efficiency in Fig. 43(b). A better bin to bin agreement is observed. As the efficiencies computed in Section 3.5 integrates out properly the rapidity dependence, we do not quote a systematic uncertainty for this effect.

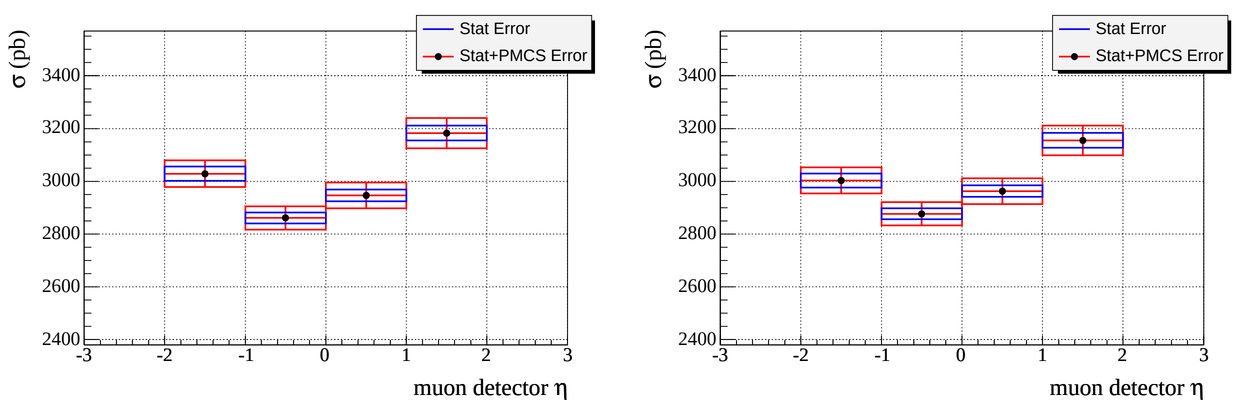

(a) section as a function of rapidity.

(b) section as a function of rapidity after correcting for isolation efficiency variation

Figure 43: Cross-section computed in different rapidity range. The weights given to the MUW_W_L2M3_TRK10 and MUW_A_L2M3_TRK10 samples are equal here. The statistical uncertainties shown on these plots are bin to bin fully uncorrelated.

7.2 Veto criteria

To check how PMCS simulates the veto on the second muon in $Z \to \mu^+\mu^-$ events, Figure 44 shows the (η, ϕ) distribution of the muon escaping the detection. In Table 14 we quote the variations of the cross-sections when the veto criteria are varied. We observe an unexpected change of 1.4% in the cross-section when the track veto is not required. Since at present there is no explanation for it, a 1.5% uncertainty is added to the cross-section measurement.

	reference		track veto only		muon veto only	
Sample	Wide	All	Wide	All	Wide	All
Number of candidates	33126	29159	34050	29892	34491	30185
$Z \to \mu^+\mu^-$ background	4.1%	4.3%	7.1%	7.2%	8.5%	8.9%
Cross-section	3020 pb	2984 pb	-0.5%	-0.5%	-0.5%	-1.4%

Table 14: Results using different veto criteria. Only the relative variation in cross-section are quoted in the last four columns.

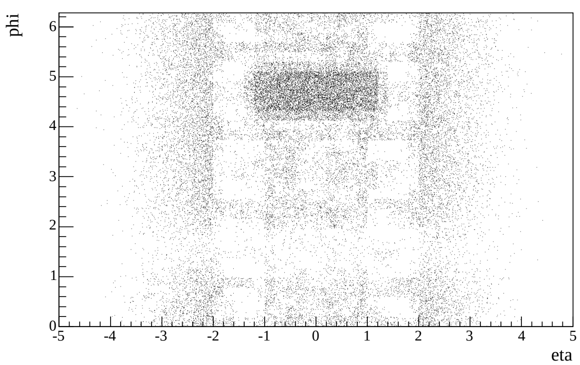

(a) muon veto only

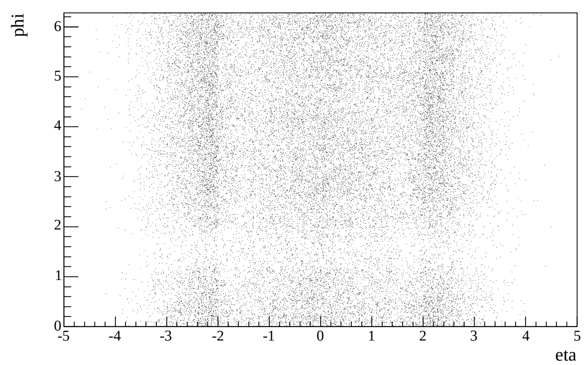

(b) track veto only

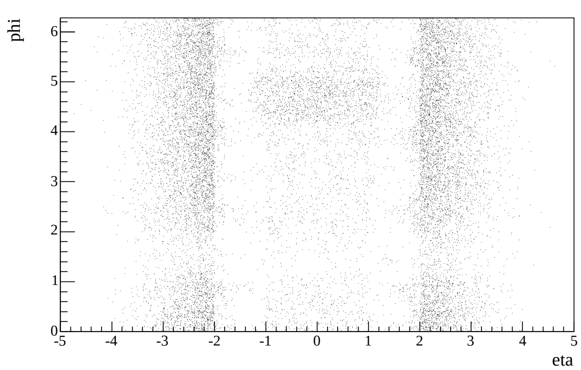

(c) both track and muon veto

Figure 44: (η, ϕ) distribution for the escaping muon in (PMCS) $Z \to \mu^+\mu^-$ events passing the selection.

7.3 Cross-section for different p_T and $\not{E}_T$ cuts

Sample	p_T,$\not{E}_T > 20$ GeV/c $M_T > 40$ GeV/c^2 Wide	All	p_T,$\not{E}_T > 25$ GeV/c $M_T > 50$ GeV/c^2 Wide	All	p_T,$\not{E}_T > 30$ GeV/c $M_T > 60$ GeV/c^2 Wide	All
Number of candidates	33126	29159	28108	24561	21055	18469
Acceptance	22.37 %	25.59%	18.81%	21.53%	14.21%	16.31%
Isolation efficiency	84.7 %	84.3 %	85.8%	84.9%	86.9%	85.3%
Electroweak background	6.7%	7.0%	5.2 %	5.4%	4.1%	4.4%
QCD background	0.7 %	0.8 %	0.4%	0.4%	0.3%	0.3%
Cross-section	3020 pb	2984 pb	-1.4%	-0.6%	-2.5%	-0.7%

Table 15: Results using different kinematical cuts. The cross-section in the last column are quoted relative to the reference cross-sections.

To test the stability of the analysis with respect to the kinematical cuts, we compared the results obtained using three sets of cuts in Table 15. The three sets are:

1. $p_T > 20$ GeV/c, $\not{E}_T > 20$ GeV and $M_T > 40$ GeV/c^2(reference cuts defined in Section 2).
2. $p_T > 25$ GeV/c, $\not{E}_T > 25$ GeV and $M_T > 50$ GeV/c^2.
3. $p_T > 30$ GeV/c, $\not{E}_T > 30$ GeV and $M_T > 60$ GeV/c^2.

Using the set of cuts 3, a relative variation of -1.9% with respect to the reference is observed for the 'wide' sample, while it is only -0.3% for the 'all' sample. This numbers have to be compared to the known effects yielding a variation in the cross-section:

- Using the set of cuts 3 suppresses $\simeq \frac{1}{3}$ of the candidate events with respect to the cuts 1. The statistical fluctuations are expected to yield a 0.4% difference between the cross-section obtained with cuts 1 and 3, for both the 'all' and the 'wide' samples.
- The IFD and cosmic backgrounds have not been reeavaluated with the cuts 3. Because of their decreasing p_T spectra, it is likely that the cuts 3 suppress these backgrounds. Hence an expected shift in the cross-section of $-0.25 \pm 0.15\%$ is expected when the cuts 3 are used.
- The QCD background is estimated to be divided by $\simeq 2$ when the cuts 3 are applied. Given the 100% uncertainty that we have quoted for this background, a 0.4% variation in the cross-section may occure.
- The impact of the uncertainty arising from the PMCS parameter α, "hadronic energy scale", was re-estimated after using the tighter set of cuts 3. It is found that the uncertainty is 1% when the set of cuts 3 is applied (it is 0.2% with the set of cuts 1).
- To propagate the effect of statistical fluctuations arising from the determination of isolation efficiency as a function of p_T, we used the full $W \to \mu\nu$ MC and generated 1000 pseudo-experiments. In each of these pseudo-experiments:

- the isolation efficiency profile histogram as a function of *pt* is randomly generated according to the error bars observed in the data (Fig. 22(a) page 25);
- the efficiency profile is fited using a S-shape function (as in Section 3.5);
- the S-shape curve is applied on the W $\rightarrow \mu\nu$ MC events satisfying the kimetical cuts to predict the acceptance.
- The number of MC W $\rightarrow \mu\nu$ events satisfying the satisfy the kinematical cuts and the isolation requirement is determined.
- A cross-section is computed, using the predited acceptance
- The difference of cross-section obtained with cuts 1 and 3 is computed.

The distribution of the differences obtained in these pseudo-experiments has a RMS of 15 pb (0.5%).

The summary of this list is given in Table 16. A shift of $\simeq -0.25\%$ and a fluctuation of 1.35% are expected. Thus the observed variations are compatible with the expectations but we conservatively quote a systematic error of 2.5% for the 'wide' region sample.

Source of fluctuation	relative change in cross-section
Number of candidates (stat)	0.4%
Isolation efficiency (stat)	0.5%
QCD background	0.4%
$\not{E}_{\mathrm{T}}$ smearing	1%
Total fluctuation (quadratic sum)	1.35 %
Source of shift	**relative change in cross-section**
IFD and cosmic	$-0.25 \pm 0.15\%$

Table 16: Summary of expected the fluctuations and shifts when the kinematical cuts are raised to $p_T > 30$ GeV/c, $\not{E}_{\mathrm{T}} > 30$ GeV and $M_T > 60$ GeV/c^2.

Appendix A: Choice of Isolation criteria and dependence with luminosity

8.4 Choice of the isolation cuts

The cuts have been chosen to ensure a reasonable signal efficiency of $\simeq 85\%$ and a low systematic error due to the QCD background. If the cuts are relaxed to get an efficiency of $\simeq 92\%$, the QCD fake isolation rate is doubled, which leads to a doubling of the systematic associated with this (this would give $\simeq 1.5\%$ error on the cross-section).

8.5 Variation with luminosity

Figures 45(a) and 45(b) present the variation as a function of the instantaneous luminosity for the track isolation cut ($\Sigma_{cone0.5}(p_T) < 1.4$ GeV/c) and the calorimeter isolation cut ($\Sigma_{halo}(E_T) <$ 2.1 GeV), respectively. These variations are fitted with linear functions. According to the fitted slopes, when the luminosity goes from 0 to $50 \times 10^{30}\text{cm}^{-2}\text{s}^{-1}$ the variation in the track isolation efficiency is $-4.2 \pm 2.3\%$ and that in the calorimeter isolation efficiency is $-10.4 \pm 1.8\%$.

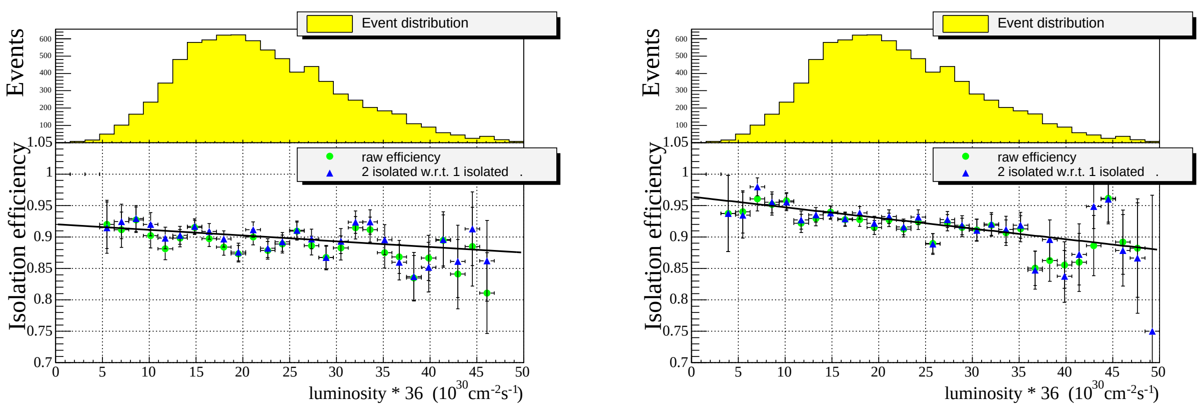

(a) Track isolation efficiency for $\Sigma_{cone0.5}(p_T) <$ 1.4 GeV/c.

(b) Calorimeter isolation efficiency for $\Sigma_{halo}(E_T) < 2.1$ GeV.

Figure 45: Measured in the $Z \to \mu^+\mu^-$ data, isolation efficiency as a function of the instantaneous luminosity per crossing (The luminosity per crossing is multiplied by 36 so that it can be compared with the overall Tevatron luminosity).

In order to remove the luminosity dependence of the isolation efficiency, the isolation cut itself is made to depend on the luminosity. For the track isolation we use the form: $\Sigma_{cone0.5}(p_T) - K_{track} \times (\mathcal{L}_I - 0.6) < 1.4$ GeV/c, where $\mathcal{L}_I$ is the instantaneous luminosity per crossing (in units of $10^{30}\text{cm}^{-2}\text{s}^{-1}$).

The value 0.6 corresponds to the average luminosity. The value of K found to provide no dependence on the luminosity is found to be $K_{track} = 0.5 \pm 0.25$.

In the same way, we use the form $\Sigma_{halo}(E_T) - K_{halo} \times (\mathcal{L}_I - 0.6) < 2.1$ GeV for the calorimeter isolation. The value of K found to provide no dependence on the luminosity is found to be

$K_{halo} = 0.75 \pm 0.15$.

The efficiencies as a function of the luminosity for the cuts $\Sigma_{cone0.5}(p_T) - 0.5 \times \mathcal{L}_I < 1.1$ GeV/c, and $\Sigma_{halo}(E_T) - 0.75 \times \mathcal{L}_I < 1.65$ GeV/c are presented in Figs. 46(a) and 46(b). We see that the isolation efficiencies are now flat as a function of the luminosity.

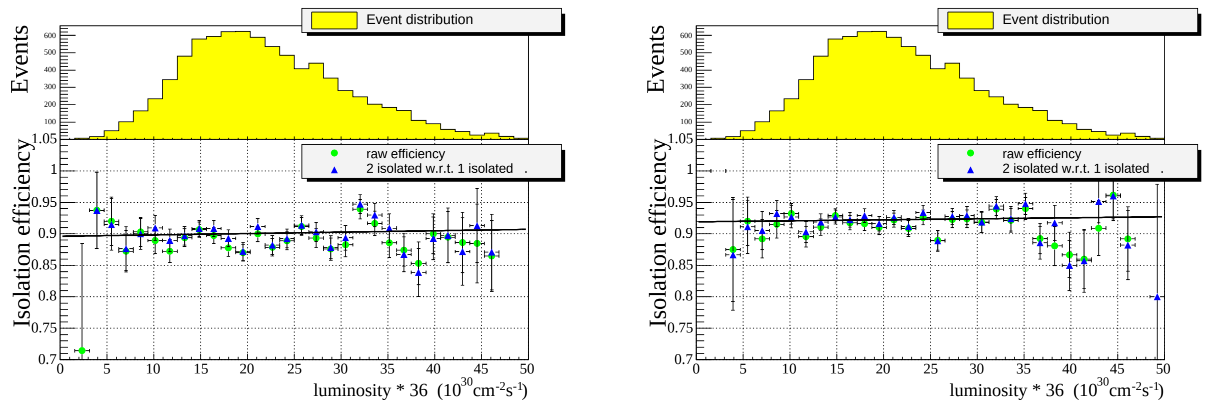

(a) Track isolation efficiency for $\Sigma_{cone0.5}(p_T) - 0.5 \times \mathcal{L}_I < 1.1$ GeV/c.

(b) Calorimeter isolation efficiency for $\Sigma_{halo}(E_T) - 0.75 \times \mathcal{L}_I < 1.65$ GeV/c.

Figure 46: Isolation efficiency as a function of the instantaneous luminosity per crossing.

In this analysis, the "and" of the calorimeter and track isolation requirement is used. Figure 47(a) presents the variation with luminosity of the isolation requirement: $\Sigma_{cone0.5}(p_T) < 1.4$ GeV/c and $\Sigma_{halo}(E_T) < 2.1$ GeV. Using a linear fit, when the luminosity goes from 0 to $50 \times 10^{30}\mathrm{cm}^{-2}\mathrm{s}^{-1}$ the efficiency variation is $-12.4 \pm 2.6\%$.

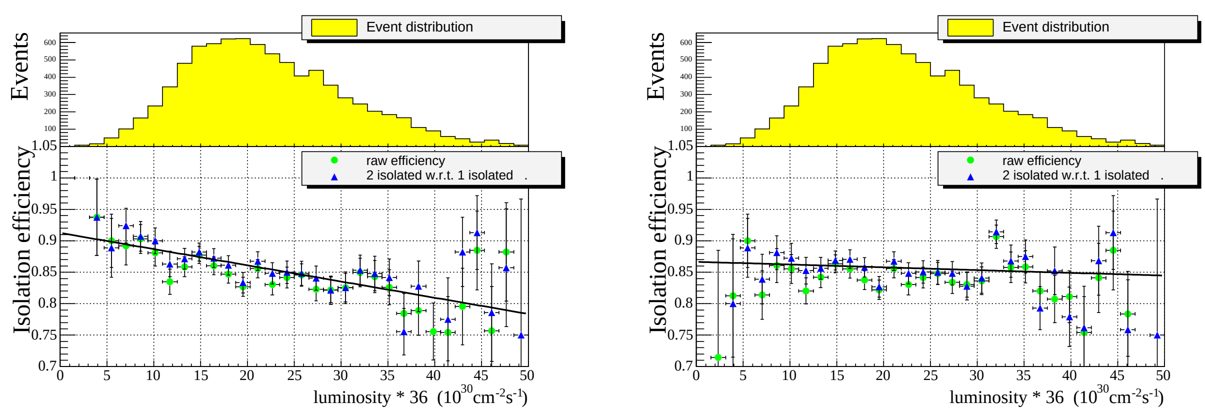

(a) Combined track and calorimeter isolation efficiency for $\Sigma_{cone0.5}(p_T) < 1.4$ GeV/c and $\Sigma_{halo}(E_T) < 2.1$ GeV/c.

(b) Combined track and calorimeter isolation efficiency for $\Sigma_{cone0.5}(p_T) - 0.5 \times \mathcal{L}_I < 1.1$ GeV/c and $\Sigma_{halo}(E_T) - 0.75 \times \mathcal{L}_I < 1.65$ GeV/c.

Figure 47: Isolation efficiency as a function of the instantaneous luminosity per crossing.

The efficiency for the isolation requirement, $\Sigma_{cone0.5}(p_T) - 0.5 \times \mathcal{L}_I < 1.1$ GeV/c and $\Sigma_{halo}(E_T) - 0.75 \times \mathcal{L}_I < 1.65$ GeV/c, is presented in Fig. 47(b). A fit to a linear function gives a variation of $-2.7 \pm 2.6\%$ when when the luminosity goes from 0 to $50\times10^{30}\mathrm{cm}^{-2}\mathrm{s}^{-1}$. As we have managed to get rid of the luminosity dependence with this definition, it is used in the analysis presented in this Note.

8.6 Cross-section using isolation efficiency varying with luminosity

As a check, we perform the cross-section measurement using the isolation requirement $\Sigma_{cone0.5}(p_T) < 1.4$ GeV/c and $\Sigma_{halo}(E_T) < 2.1$ GeV and compare it to the results presented in Section 6.1, obtained using $\Sigma_{cone0.5}(p_T) - 0.5 \times \mathcal{L}_I < 1.1$ GeV/c and $\Sigma_{halo}(E_T) - 0.75 \times \mathcal{L}_I < 1.65$ GeV/c.

The isolation efficiency varying with p_T is measured using the $Z \rightarrow \mu^+\mu^-$ peak as described in Section 3.5. The known variation with instantaneous luminosity is therefore averaged over the $Z \rightarrow \mu^+\mu^-$ sample. As this sample corresponds to the same period of data taking, we expect this average to be a good estimate of the true average $W \rightarrow \mu\nu$ isolation efficiency. The fake isolation rate is determined in the same way as described in Section 5.2. We find the same fake isolation rate. The results after applying all cuts and recomputing the backgrounds are summarised in Table 17.

Sample	MUW_W_L2M3_TRK10	MUW_A_L2M3_TRK10
Number of candidate events	33588	30028
Isolation efficiency	84.0 %	85.8 %
Electroweak background	7.1%	7.2%
QCD background	0.7 %	0.8 %
Variation in cross-section relative to the reference result (Section 6.1)	-0.17%	-0.1%

Table 17: Result summary with the isolation definition: $\Sigma_{cone0.5}(p_T) < 1.4$ GeV/c and $\Sigma_{halo}(E_T) < 2.1$ GeV.

The variation in the cross-section with respect to the results in Section 6.1 are negligible. Therefore we do not modify the uncertainties quoted in Section 6.1.

References

[1] M. Agelou *et al*, DØ Note 4128, 'Measurement of the Inclusive $W \to \mu\nu$ Cross-Section in $p\bar{p}$ Collisions at $\sqrt{s} = 1.96$ TeV'.

[2] See http://www-d0.fnal.gov/phys_id/muon_id/d0_private/certif/p14/index.html#certification%20crit for the definition of meon and M. Kado, DØ Note 4070, 'Muon Isolation Studies'.

[3] http://www-d0.fnal.gov/Run2Physics/cs/index.html.

[4] T. Edwards *et al*, DØ Note 4328, "The Update DØ Luminosity Determination - Short Summary.

[5] File of beam spot position is provided by G. Borrisov.

[6] Emily Nurse and Paul Telford, DØ Note 4573, 'Measurement of the Cross section for Inclusive Z Production in Di-muon Final States at $\sqrt{s} = 1.96$ TeV'.

[7] http://www-d0.fnal.gov/d0dist/dist/packages/wzreco/devel/doc/wzreco.ps
http://www-d0.fnal.gov/d0dist/dist/packages/muo_cert/devel/doc/muo_cert.ps.

[8] Christophe Clement, Frederic Déliot, Martijn Mulders, Stefan Soldner-Rembold, for D0 Muon Algo and Muon ID groups, DØ Note 4091, 'Content of the p13 muon thumbnail'.

[9] Benoit Clément *et al*, DØ Note 4159, 'System D, or how to get signal, background and their efficiencies with real data'.

[10] Sarah Eno and Marco Verzocchi, DØ Note 4097, 'Status of the Fast Simulation, PMCS'.

[11] P Telford*et al*, DØ Note 4297, 'Retuning of pmcs_chprt to P13 and P14 data' .

[12] D. Chapin *et al*, DØ Note 4403, 'Measurement of $Z \to ee$ and $W \to e\nu$ Production Cross Sections with $|eta| < 2.3$'.

[13] T Sjöstrand et al, Computer Physics Commun 135 (2001) p238, 'Pythia v6.2 Physics and Manual'.

[14] J Pumplin et al, hep-ph/0201195 'New Generation of Parton Distributions with Uncertainties from Global QCD Analysis'.

[15] U Yang and Y Kim, 'ISR Studies on Drell-Yan', Fermilab MC Workshop (2003)
http://cepa.fnal.gov/patriot/mc4run2/MCTuning/031204/unki.pdf.

[16] B. Tiller and T. Nunneman, DØ Note **4660** (2004).

[17] S. Frixione and B.R. Weber, J.H.E.P. **206** 029 (2002).
S. Frixione, P. Nason and B.R. Weber, J.H.E.P. **308** 007 (2003).

[18] C. R. Hamberg, W.L. van Neerven and T. Matsuura, Nucl. Phys. B359 (1991) 343.

[19] First Measurements of Inclusive W and Z Cross Sections From Run II of the Tevatron Collider, the CDF Collaboration, hep-ex/0406078, submitted to Phys.Rev.Lett.